Fluid-Assisted Deformation and Strain Localization in the Cooling Mantle Wedge of a Young Subduction Zone (Semail Ophiolite)

Cécile Prigent, S. Guillot, Philippe Agard, Benoit Ildefonse

Journal of Geophysical Research: Solid Earth

RESEARCH ARTICLE
10.1029/2018JB015492

Key Points:
- The base of the Semail ophiolite is a proxy for a mantle wedge deforming and interacting with subduction fluids right above a hot plate interface
- Fluid/peridotite interaction leads to dissolution/precipitation processes, grain size reduction, and peridotite weakening at short time scales
- Such peridotite weakening explains intense strain localization within the ductile mantle wedge and the observed switch in the subduction interface regime

Supporting Information:
- Supporting Information S1

Correspondence to:
C. Prigent,
cprigent@udel.edu

Citation:
Prigent, C., Guillot, S., Agard, P., & Ildefonse, B. (2018). Fluid-assisted deformation and strain localization in the cooling mantle wedge of a young subduction zone (Semail ophiolite). *Journal of Geophysical Research: Solid Earth*, *123*, 7529–7549. https://doi.org/10.1029/2018JB015492

Received 17 JAN 2018
Accepted 15 AUG 2018
Accepted article online 24 AUG 2018
Published online 21 SEP 2018

Fluid-Assisted Deformation and Strain Localization in the Cooling Mantle Wedge of a Young Subduction Zone (Semail Ophiolite)

C. Prigent[1,2], S. Guillot[1], P. Agard[3], and B. Ildefonse[4]

[1]University Grenoble Alpes, University Savoie Mont Blanc, CNRS, IRD, IFSTTAR, ISTerre, Grenoble, France, [2]Now at Department of Geological Sciences, University of Delaware, Newark, DE, USA, [3]Sorbonne Universités, UPMC University Paris 06, CNRS, Institut des Sciences de la Terre de Paris, Paris, France, [4]Géosciences Montpellier, CNRS, Université de Montpellier, Université des Antilles, Montpellier, France

Abstract This study reports on feedback mechanisms between fluid migration, ductile deformation, and strain localization processes in an incipiently forming mantle wedge: the basal banded unit of the Semail ophiolite. These peridotites were located right above the plate interface during intraoceanic subduction infancy that ultimately led to ophiolite obduction. During this stage, they were affected by coeval ductile deformation, forming (proto)mylonites at ~900–800 °C to ultramylonites at ~700 °C, and interaction with subduction fluids. From the petrological and microstructural study of these hydrated peridotites and their protolith (preserved lenses of porphyroclastic tectonites), we show that peridotite interaction with hydrous fluids triggered dissolution/precipitation processes. Dissolution of coarser grains and precipitation of new and smaller ones (mainly pyroxenes, spinel, and amphibole) resulted in a drastic grain size reduction, phase mixing and a switch from olivine dislocation to grain size sensitive creep in (proto)mylonites. Data also evidence a feedback process of fluid focusing in actively deforming shear zones. This rapid switch in olivine deformation mechanism, driven by subduction fluid-peridotite interaction, triggered an intense weakening of the peridotites at ~900–800 °C and a transition from a mechanically decoupled to coupled plate interface (as witnessed by the detachment and underplating of a high-temperature metamorphic sole to the base of the ophiolite). It also explains the intense strain localization (<1-km-thick shear zone) along this ductile portion of the plate interface. Considering that similar mechanisms take place in mature subduction zones, they may explain plate interface coupling at subarc depths in worldwide subduction zones.

1. Introduction

Hydration of mantle wedge peridotites by fluids (and/or hydrous melts) released by downgoing plates is expected to decrease mantle strength during subduction (Chernak & Hirth, 2010; Hilairet et al., 2007; Hirth & Kohlstedt, 2003). Such peridotite weakening is considered to be critical for subduction initiation (Regenauer-Lieb et al., 2001), for influencing middle- to long-term mechanical coupling of the subduction interface (Agard et al., 2016; Wada et al., 2008), and for earthquake nucleation (Obara, 2002; Peacock & Hyndman, 1999).

At $T < 700$ °C, hydration of peridotites mainly triggers serpentine crystallization, a rheologically weak mineral (Chernak & Hirth, 2010; Hilairet et al., 2007; Raleigh & Paterson, 1965). From geological and geophysical arguments, the presence of serpentinized peridotites in the fore-arc mantle wedge has been proposed as an explanation to the (partial) decoupling of the subduction interface in this zone (Bostock et al., 2002; Fryer et al., 1999; Hirth & Guillot, 2013; Hyndman & Peacock, 2003). Deeper down (from 70 to 80 km in mature subduction zones), the subducting plate and the overlying hydrated mantle wedge are thought to be coupled again and dragged down together (Furukawa, 1993; Wada & Wang, 2009), thereby leading to asthenospheric mantle wedge return flow and changes in overriding plate thermal structure (Abers et al., 2017; Kelemen et al., 2003; Peacock, 1996).

Mechanical coupling at the interface and, in particular, the rheology of mantle wedge peridotites over the stability of serpentine (i.e., $T > 550$–700 °C, depending on pressure) therefore exerts a key control on the dynamics and thermal regime of subduction zones (Arcay et al., 2007; Syracuse et al., 2010; van Keken et al., 2002). However, the rheological behavior (i.e., deformation mechanisms, strain localization, and overall strength) of this ductile mantle wedge is not well constrained (e.g., Agard et al., 2016). The origin of the subarc

mantle wedge low seismic velocities revealed by geophysics remains debated (Kawakatsu & Watada, 2007; Reynard, 2013; Wada & Wang, 2009), and nonserpentinized mantle wedge peridotites exhumed from suture zones or as xenoliths are scarce and do not preserve structural relationship to the subduction interface.

An alternative approach is to study the exhumed mantle section of ophiolites, which are fragments of oceanic lithosphere once located above an intraoceanic subduction zone (Dewey, 1976). The presence of metamorphosed crustal rocks (amphibolitic to granulitic metamorphic soles) immediately below the mantle base of ophiolites indeed attests that parts of the downgoing plate were sheared, heated up, and accreted to the ophiolite base during the first stage of intraoceanic subduction (Figure 1a; Agard et al., 2016; Dewey & Casey, 2013; Spray, 1984; Wakabayashi & Dilek, 2003). In the Semail ophiolite, the basal ophiolitic mantle and the metamorphic sole below were tectonically juxtaposed, deformed at temperature conditions of ~900–650 °C (Boudier et al., 1988; Boudier & Coleman, 1981; Gnos, 1998; Gnos & Kurz, 1994; Lippard et al., 1986; Searle, 1980; Soret et al., 2017), and exhumed together during early subduction (Agard et al., 2016). Prigent et al. (2018) have shown that these basal mylonitic peridotites are enriched in fluid-mobile elements and in amphibole, suggesting subduction fluid release from the downgoing plate and fluid/peridotite interaction during mylonitic deformation.

The base of the Semail ophiolite is therefore a good proxy to examine ductile deformation of a mantle wedge located and interacting with fluids immediately above a warm (~650-900 °C) subduction interface. Based on a petrological and microstructural analysis of these basal peridotites, combined with the sample geochemical characterization from Prigent et al. (2018), the present study aims at understanding the influence of fluid/mantle interaction processes on (1) peridotite rheology, (2) strain accommodation within the mantle wedge, and (3) the regime of the subduction plate interface.

2. Petrological and Tectonic Setting

A detailed description of the geological setting of the Semail ophiolite and/or of the ophiolite emplacement is beyond the scope of the present contribution, and the interested reader is referred to the abundant literature on this subject (e.g., Agard et al., 2007, 2016; Ceuleneer et al., 1988; Coleman, 1981; Le Mée et al., 2004; Morris et al., 2016; Nicolas et al., 2000; Rioux et al., 2016; Searle & Cox, 2002). In the first ~200–500 m above the fossil plate interface (i.e., above the contact with the metamorphic sole), the ophiolitic mantle displays structural characteristics that differ from the overlying ophiolitic mantle section (Nicolas et al., 2000). Basal mantle peridotites form a highly foliated *banded unit* (Searle, 1980), displaying centimetric to metric lithological alternations of harzburgites, lherzolites, dunites, and pyroxenites (Boudier & Coleman, 1981; Lippard et al., 1986; Searle, 1980; Takazawa et al., 2003). Detailed structural works performed on the whole ophiolitic mantle section have revealed that the ductile mylonitic deformation of this basal banded unit took place at relatively low temperature (LT deformation) and is superimposed on a higher temperature *asthenospheric* deformation (HT deformation) attributed to the accretion process of the main magmatic sequence of the ophiolite (Figure 1b; Boudier et al., 1988; Nicolas et al., 2000). This HT mantle is also crosscut by vertical mylonitic shear zones interpreted as developing coevally with the banded unit during the LT event (e.g., Boudier et al., 1988). In contrast to the basal banded unit, which has been studied only very recently from a rheological point of view in the Kwar Fakkan massif (Ambrose et al., 2018), the vertical shear zones have been thoroughly characterized by microstructural studies (Linckens, Herwegh, & Müntener, 2011, Linckens, Herwegh, Müntener, & Mercolli, 2011; Michibayashi et al., 2000, 2006; Michibayashi & Mainprice, 2004). The temperature of the LT deformation event, affecting high-temperature (~1200 °C) porphyroclastic tectonites, has been estimated at ~900–800 °C for the (proto) mylonitic deformation and down to ~700 °C for the ultramylonitic deformation (Linckens, Herwegh, & Müntener, 2011).

The metamorphic sole of the Semail ophiolite crops out all along the ophiolite at its base (Figure 1b) and exhibits tectono-metamorphic characteristics similar to those of other metamorphic soles worldwide (Agard et al., 2016; Soret et al., 2017). When the sequence is complete, the metamorphic sole comprises at least two units: an upper (amphibolitic to granulitic) HT sole and a lower (greenschist facies) LT sole. The HT sole is mainly composed of sheared metabasalts metamorphosed at ~800 ± 50 °C and 1.0 ± 0.2 GPa (Agard et al., 2016; Cowan et al., 2014; Ghent & Stout, 1981; Gnos, 1998; Hacker & Mosenfelder, 1996; Searle, 1980; Searle & Malpas, 1980; Soret et al., 2017), corresponding to ~30 km depth. The LT sole comprises far more metasediments and shows lower pressure (P)-T peak conditions at ~600 ± 50 °C and 0.5 ± 0.1 GPa (Agard et al., 2016;

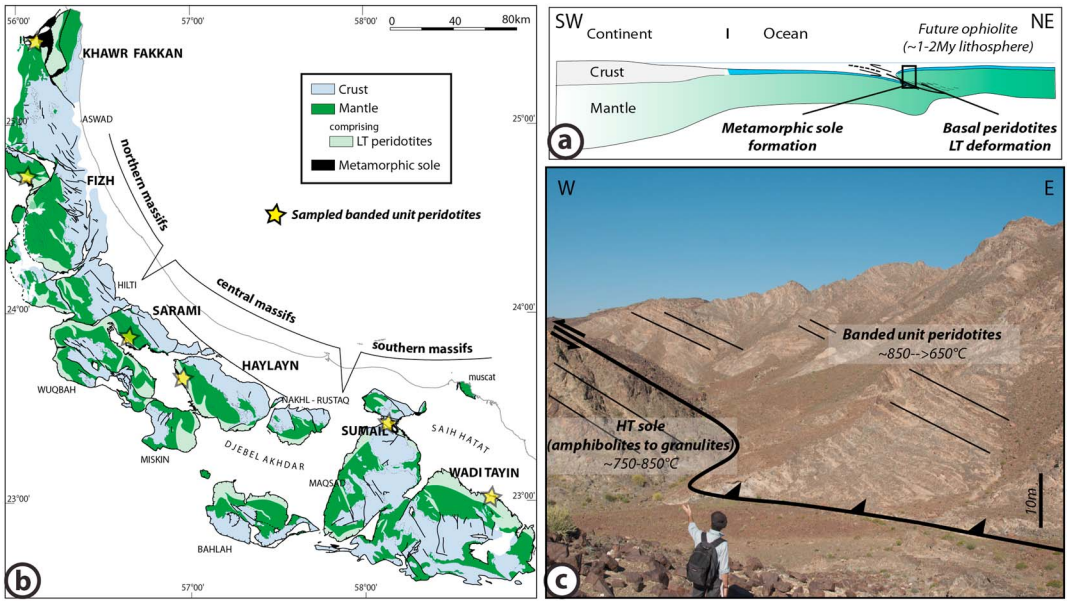

Figure 1. (a) Geodynamic sketch of the setting of intraoceanic subduction infancy. This stage results in the (de)formation of the HT (amphibolitic to granulitic) metamorphic sole and the LT deformation of the ophiolite basal peridotites resulting in the formation of the banded unit. (b) Simplified geological map of the Semail ophiolite featuring the main petrological units and highlighting the location of the LT mylonitic basal peridotites of the ophiolite section (map modified after Nicolas et al., 2000) and of analyzed samples. (c) Field view of the basal contact between the HT sole and the overlying ophiolitic banded unit. Note the concordant foliation of the two units. HT = high temperature; LT = low temperature.

Bucher, 1991; Gnos, 1998; Soret et al., 2017), corresponding to a depth of ~15 km. HT and LT units at the base of the Semail ophiolite are interpreted as resulting from deformation, heating up and slicing off the downgoing plate during the first stages of intraoceanic subduction (Agard et al., 2016; Searle & Cox, 1999), long before ophiolite emplacement onto the Arabian continent in the late Cretaceous. HT sole metamorphism has been dated at 94–95 Ma, supporting the view that the overlying lithosphere was still young (~1–2 My old) and hot when the HT sole formed (Goodenough et al., 2010; Hacker et al., 1996; Rioux et al., 2013, 2016; Warren et al., 2005).

As the deformation patterns (foliation, lineation, and folds) and temperature of banded unit mylonitic peridotites appear to be similar to those of the underlying high-temperature (HT) sole (Figure 1c), their deformation was attributed to the same tectonic stage (Boudier et al., 1988; Boudier & Coleman, 1981; Nicolas et al., 2000; Searle, 1980; Searle & Malpas, 1982), that is, deformation and cooling of the basal ophiolitic mantle, located immediately above the interface, during early subduction and metamorphic sole accretion (Figure 1a). Petrological and geochemical studies suggest that basal peridotites were affected by metasomatic processes during this deformation. Metasomatism is evidenced by constitutive mineral enrichment in fluid mobile elements (especially boron; Khedr et al., 2013, 2014; Prigent et al., 2018; Yoshikawa et al., 2015), in heavy boron (^{11}B) compared to ^{10}B (Prigent et al., 2018), and crystallization of metasomatic minerals: amphibole and secondary olivine, clinopyroxene, orthopyroxene, and spinel (Ambrose et al., 2018; Khedr et al., 2013, 2014; Prigent et al., 2018). These authors relate the cryptic and modal metasomatism of basal peridotites to fluids released by dehydration of the underlying metamorphic sole. From geochemical arguments, Prigent et al. (2018) propose that the interaction of basal peridotites with these fluids started during the protomylonitic deformation stage (at ~850 °C), coevally with the formation and dehydration of the underlying HT sole.

3. Sample Selection and Methods

Banded unit peridotites directly overlying the HT sole were sampled across several ophiolite transects (from the Kwar Fakkan to the Wadi Tayin massifs; Figure 1b) in order to characterize their mechanical behavior and the interplay between fluid percolation, ductile deformation, and strain localization processes. Deformation

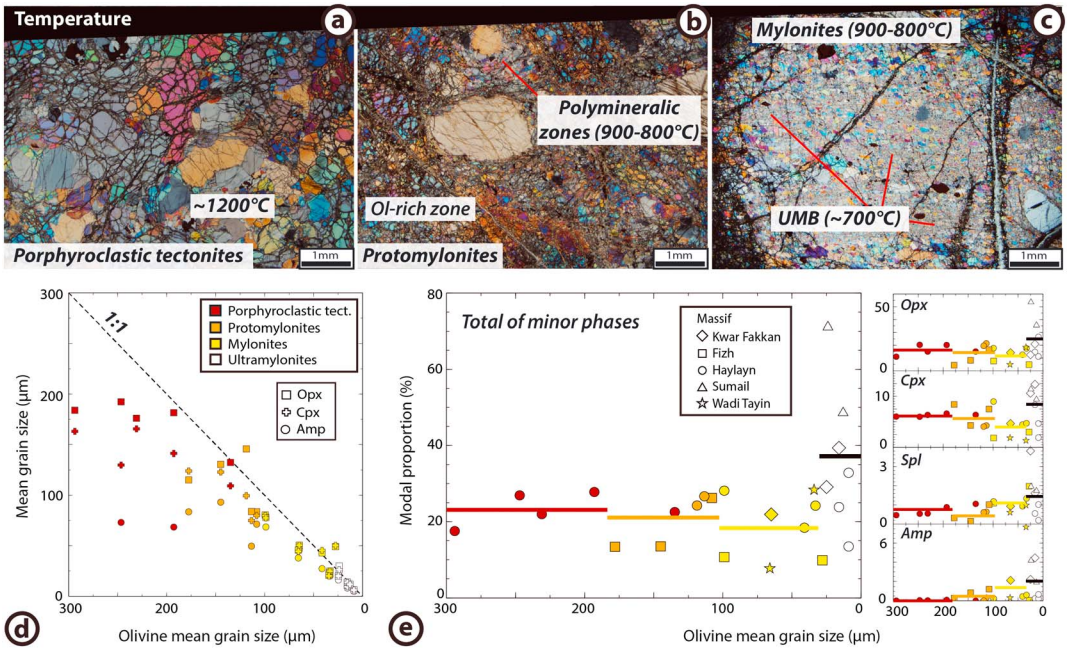

Figure 2. (a–c) Optical microphotographs showing the change in banded unit peridotite microstructures associated with increasing low temperature deformation and cooling during subduction infancy: from the protolith (porphyroclastic tectonites), protomylonites, mylonites to ultramylonites or ultramylonitic bands (UMB). (d) Evolution of orthopyroxene (Opx), clinopyroxene (Cpx) and amphibole (Amp) mean grain size as a function of olivine mean grain size in analyzed EBSD maps. (e) Evolution of minor phase abundance—Opx, Cpx, spinel (Spl), and Amp–during increasing deformation.

of the banded unit is heterogeneous along strike the ophiolite (Figures 2a–2c and Table 1). The banded unit is generally composed of centimetric to decimetric (proto)mylonitic to ultramylonitic shear zones/bands. Along the Haylayn cross section, however, these LT shear zones wrap around preserved decimetric lenses of high-temperature porphyroclastic tectonites. We selected 20 samples showing different stages of deformation, from porphyroclastic to ultramylonitic microstructures from the different massifs, to perform detailed petrological and microstructural analysis. One mylonitic shear zone located in Haylayn massif is more thoroughly documented in order to further assess the evolution of peridotites across a well-defined strain gradient. The investigated sample set (Table 1) comprises six porphyroclastic tectonites (Figure 2a), six protomylonites (one with ultramylonitic bands, UMB, sample SE13-37B; Figure 2b), seven mylonites (three with UMB, samples SE13-37B, SE14-06B, and SE13-113; Figure 2c), and one ultramylonite (sample SE11-01). Sample classification, established after petrographic observation, follows that of Linckens, Herwegh, and Müntener (2011).

Petrological and microstructural analyses were carried out on 30 µm-thick polished thin sections using SEM (scanning electron microscope) imaging and coupled Electron BackScattered Diffraction (EBSD)/Energy Dispersive Spectroscopy (EDS) mapping. EBSD measurements were performed on a Camscan Crystal Probe X500FE SEM at Geosciences Montpellier (France) using a 15 kV acceleration voltage. EBSD/EDS map step size (35 to 1 µm) was adjusted to sample minimum grain size. At each step, phase identification (olivine, clinopyroxene, orthopyroxene, amphibole, or spinel) and crystallographic orientations were acquired in automatic mode from the diffraction pattern and phase crystallographic parameters. Indexation rates for the raw maps range from 95% to 50%, depending on the degree of serpentinization. Raw maps were first processed using the Channel 5 software (HKL Oxford Instruments 5) in order to remove isolated pixels, correct errors due to olivine hexagonal pseudosymmetry, and fill nonindexed pixels surrounded by five or six identical (phase and orientation) neighbors. Then, the MTEX free toolbox for Matlab (Bachmann et al., 2010) was used to analyze the data and calculate phase modal proportion, grain size, shape preferred orientation (SPO), crystallographic preferred orientation (CPO), and misorientation distributions. Grain boundaries (in black on EBSD maps below) were identified as the boundaries between two different phases or between two adjacent pixels of the same phase

Journal of Geophysical Research: Solid Earth

10.1029/2018JB015492

Table 1

Sample Location, Rock Textures, and Main EBSD Map Results: Mean Grain Size, Percentage Area, CPO Strength, Geometry, and Number of Grains of the Different Phases

			Location			Mean grain size (μm)				Phase percentage area						J-index			M-index			FIA	Number of map grains		
Zone texture	Massif	Sample	Latitude	Longitude	Zone	ol	opx	cpx	amph	ol	opx	cpx	amph	spl	Σ minor phases	ol	opx	cpx	ol	opx	cpx	ol	ol	opx	cpx
Porphyroclastic	Haylayn	SE14-04	25 39 01.6	58 56 21.8		247	192	130	73	63.2	20.3	6.0	0.1	0.5	26.9	2.37	2.51	3.27	0.09	0.09	0.02	-	1,223	601	505
		SE14-05	25 39 00.0	58 56 21.6		294	176	166	-	75.1	11.0	6.0	0.0	0.5	17.5	2.3	1.61	1.96	0.10	0.03	0.02	119	1,870	841	676
		SE14-07	24 38 59.4	57 56 21.4		231	184	163	-	67.5	15.0	6.3	0.0	0.5	22.0	1.79	1.55	2.13	0.07	0.04	0.03	112	2,255	708	454
		SE13-39	22 38 56.4	57 56 18.3		193	182	141	68	55.7	20.2	6.6	0.1	0.9	27.8	2.13	1.47	1.71	0.09	0.03	0.03	121	2,902	1,044	836
		SE13-41	25 38 52.2	58 56 16.2		185	138	92	85	59.1	14.4	1.7	1.3	0.3	17.7	2.33	1.57	2.19	0.12	0.04	0.02	-	5,666	2,035	857
		SE13-38	23 38 58.9	56 56 20.3		135	133	109	-	39.4	15.1	6.4	0.0	1.1	22.5	1.93	1.30	1.48	0.08	0.01	0.01	86	4,609	1,314	1,149
Protomylonitic	Fizh	SE13-83	24 42 00.5	56 03 56.1		145	131	123	93	51.7	8.2	4.3	0.9	0.1	13.5	1.85	-	-	0.07	-	-	51	1,632	170	184
		SE13-82	24 41 58.3	56 03 55.2		178	115	124	84	69.6	4.4	8.4	0.3	0.3	13.4	2.37	1.92	1.80	0.12	0.03	0.03	87	2,422	291	691
		SE13-81	24 41 55.7	56 03 53.3		108	84	80	71	66.4	16.5	7.5	1.2	1.0	26.3	1.48	1.44	1.97	0.04	0.01	0.03	119	2,940	1,084	783
	Haylayn	SE14-06A	26 39 01.0	59 56 21.7		113	84	75	50	64.1	21.5	4.3	0.3	0.6	26.7	1.48	1.28	1.86	0.04	0.02	0.02	57	3,393	1,995	593
		SE13-33	23 38 48.6	56 56 10.4		119	146	100	-	29.5	19.6	4.1	0.0	0.6	24.3	1.92	1.37	1.51	0.07	0.02	0.01	-	5,529	1,469	1,059
Mylonitic	KF	SE13-121	25 26 50.4	56 05 44.5		65	51	50	46	46.7	14.2	4.7	2.1	0.9	21.9	1.41	1.31	-	0.03	0.01	-	-	1,780	893	243
	Fizh	SE13-80	24 41 54.3	56 03 52.4		99	80	80	-	41.3	7.7	1.8	0.1	1.1	10.7	1.56	1.42	-	0.05	0.01	-	95	2,117	523	148
		SE13-77	24 41 52.9	56 03 52.8		28	49	50	-	35.0	4.8	3.0	0.0	2.0	9.8	1.65	1.77	-	0.05	0.04	-	122	2,251	490	265
	Haylayn	SE13-37A	23 39 01.0	56 56 21.6	2	99	78	78	69	57.7	17.8	9.0	0.2	1.2	28.2	1.31	1.16	1.22	0.03	0.02	0.01	110	26,751	6,322	2,469
		SE13-37B	23 39 01.0	56 56 21.6	2	41	43	45	27	70.9	12.6	4.5	0.4	0.9	18.4	1.2	1.15	1.31	0.02	0.01	0.01	112	12,137	3,281	1,802
		SE14-06B	27 39 01.0	60 56 21.7	1	33	25	25	20	69.1	17.6	4.7	0.6	1.3	24.2	1.11	1.17	1.25	0.01	0.02	0.01	112	13,473	7,340	1,957
	WT	WT11-10	23 02 17.7	58 40 54.4	2	66	46	44	38	69.3	4.9	1.8	0.3	0.6	7.7	1.14	2.15	1.37	0.01	0.01	0.02	83	4,502	634	305
					1	34	21	20	24	62.0	18.4	1.3	7.7	1.0	28.4	1.16	1.41	-	0.01	0.03	-	-	3,103	2,232	178
Ultramylonitic/	Haylayn	SE13-37B	23 39 01.0	56 56 21.6	1	16	13	10	8	72.6	14.7	8.3	0.2	0.6	23.8	1.17	1.32	-	0.01	0.02	0.03	100	3,964	1,602	403
UMB		SE13-37A	23 39 01.0	56 56 21.6	1	9	7	6	5	47.9	11.2	1.9	0.2	0.2	13.5	1.08	1.20	1.47	0.00	0.01	0.01	137	3,206	1,969	1,141
		SE14-06B	27 39 01.0	60 56 21.7	2	9	7	6	6	60.2	26.5	4.7	0.7	1.0	32.9	1.09	1.26	1.67	0.00	0.02	0.01	-13	3,416	2,871	646
	KF	SE13-113	25 26 30.2	56 07 20.1	1	16	14	14	10	54.9	20.9	12.3	4.5	1.6	39.3	1.25	1.23	1.40	0.02	0.01	0.01	-	6,859	2,889	2,127
					2	25	20	20	16	62.5	12.5	10.6	2.2	3.8	29.1	1.23	1.15	1.27	0.03	0.01	0.01	83	10,910	3,618	3,412
	Fanjah	SE11-01	23 23 49.8	58 08 37.0	1	24	30	26	24	25.2	53.6	11.4	4.2	2.0	71.1	1.11	1.14	2.17	0.00	0.01	0.01	-	3,237	2,427	823
					2	13	12	12	10	47.3	35.5	9.4	1.9	1.7	48.6	1.07	1.23	1.44	0.00	0.02	0.01	−4	7,468	5,147	1,741

Note. CPO strength was estimated by calculating the M-index (Skemer et al., 2005) and the J-index (Mainprice & Silver, 1993), taking into account the average orientation of grains. CPO geometry for olivine was characterized using the FIA (Michibayashi et al., 2016) ;- = not calculated, not present, or not enough measurements. KF = Kwar Fakkan; WT = Wadi Tayin; ol = olivine; opx = orthopyroxene; cpx = clinopyroxene; amph = amphibole; spl = spinel; EBSD = Electron BackScattered Diffraction; CPO = crystallographic preferred orientation; FIA = fabric-index angle.

with >10° of crystallographic misorientation. Grains with less than five pixels were discarded to eliminate potential misindexing.

To characterize mineral CPO, the orientation distribution function was calculated using a half width of the *de la Vallée Poussin* kernel of 10° (Mainprice et al., 2014) and the mean orientation of each grain to avoid overrepresentation of coarser grains. Phases mapped with <200 grains were not considered in order to get representative mineral fabrics (Table 1; Ismail & Mainprice, 1998). CPO, reported in Figure S1 in the supporting information, is plotted on lower hemisphere, equal area pole figures and contoured at multiples of a uniform distribution. We used the eigen analysis described in Mainprice et al. (2014) to calculate for each mineral crystallographic axis the eigenvectors E_i of its orientation tensor. E_1 represents the preferred orientation of the axis. We also calculate the fabric-index angle of Michibayashi et al. (2016) for olivine, using the elastic coefficients of Abramson et al. (1997), and a density of 3.355 g/cm^3 to calculate seismic velocities. To quantify mineral CPO strength, we use two different indexes, both decreasing with decreasing fabric strength: the M-index (Skemer et al., 2005) and the J-index (Mainprice & Silver, 1993). The M-index is equal to 1 for a single crystal and decreases to 0 for a random fabric, while the J-index ranges from infinite (single crystal) to 1 (random fabric).

Intragranular misorientation is characterized by plotting the difference in orientation between each pixel to the mean orientation of the grain (Mis2mean). Low-angle (2–10°) misorientations and the distribution of corresponding misorientation rotation axes are shown on inverse pole figures to identify dominant rotation axes (Figure S1).

Boron separation and analyses were made at LHyGeS (University of Strasbourg, France). The boron extraction procedure, adapted from Lemarchand et al. (2012), is detailed in Prigent et al. (2018). Sample isotopic ratios were then measured by Multicollector-Inductively Coupled Plasma Mass Spectrometer (MC-ICPMS) on a Thermo Scientific Neptune. The full set of results is reported and discussed in Prigent et al. (2018). Herein, we only report the boron composition of samples taken along the well-documented mylonitic shear zone in the Haylayn massif.

4. Results

4.1. Grain Size and Mineralogy Evolution

Samples are spinel lherzolites (clinopyroxene >5%) or cpx-harzburgites (clinopyroxene >2%) and may contain amphibole (magnesio-hornblende to pargasite; Table 1). Olivine and pyroxene mean grain size progressively decreases from porphyroclastic tectonites (~300 μm) to ultramylonites/UMB (~5 μm; Figure 2d). Amphibole grain size is similar in porphyroclastic tectonites and protomylonites but markedly decreases in mylonites and ultramylonites/UMB. Except in some area of the ultramylonitic sample from Fanjah, olivine is systematically the dominant indexed phase (Table 1). The average proportion of minor phases slightly decreases from porphyroclastic tectonites to mylonites but is the highest in the ultramylonite and UMB (Figure 2e). Along the Haylayn cross section, no significant variation is observed with increasing deformation. While the modal amount of every minor phase increases in the ultramylonite/UMB, amphibole is the only phase whose proportion progressively increases with increasing deformation (Figure 2e).

4.2. Petrography and Microstructures

In porphyroclastic tectonites, orthopyroxene and olivine porphyroclasts (up to a few millimeters) have irregular grain boundaries. Grain aspect ratios are up to 1:5 for orthopyroxene and 1:4 for olivine (Figure 2a). Both phases show important intracrystalline deformation with undulose extinction and kink bands. In some samples, orthopyroxene and clinopyroxene are partly overgrown by amphibole.

Two distinct domains can be recognized in protomylonites: a coarser-grained olivine-rich domain and a finer-grained polymineralic one (Figures 2b and 3a–3c). In coarser-grained zones, olivine grains may also have grain sizes up to a few millimeters and irregular grain boundaries (Figures 2b and 3a). Olivine commonly shows triple junctions and is in places strongly elongated with aspect ratios of up to 1:6 for the coarse grains. In these zones, olivine is locally associated with spinel and sometimes orthopyroxene and clinopyroxene porphyroclasts. Olivine and pyroxene porphyroclasts show intense intracrystalline deformation with numerous kink bands, undulose extinction, and bent exsolution lamellas in pyroxene (Figure 3c). In these protomylonites, drastic grain size reduction (to grains <300 μm) mainly occurs around pyroxene porphyroclasts

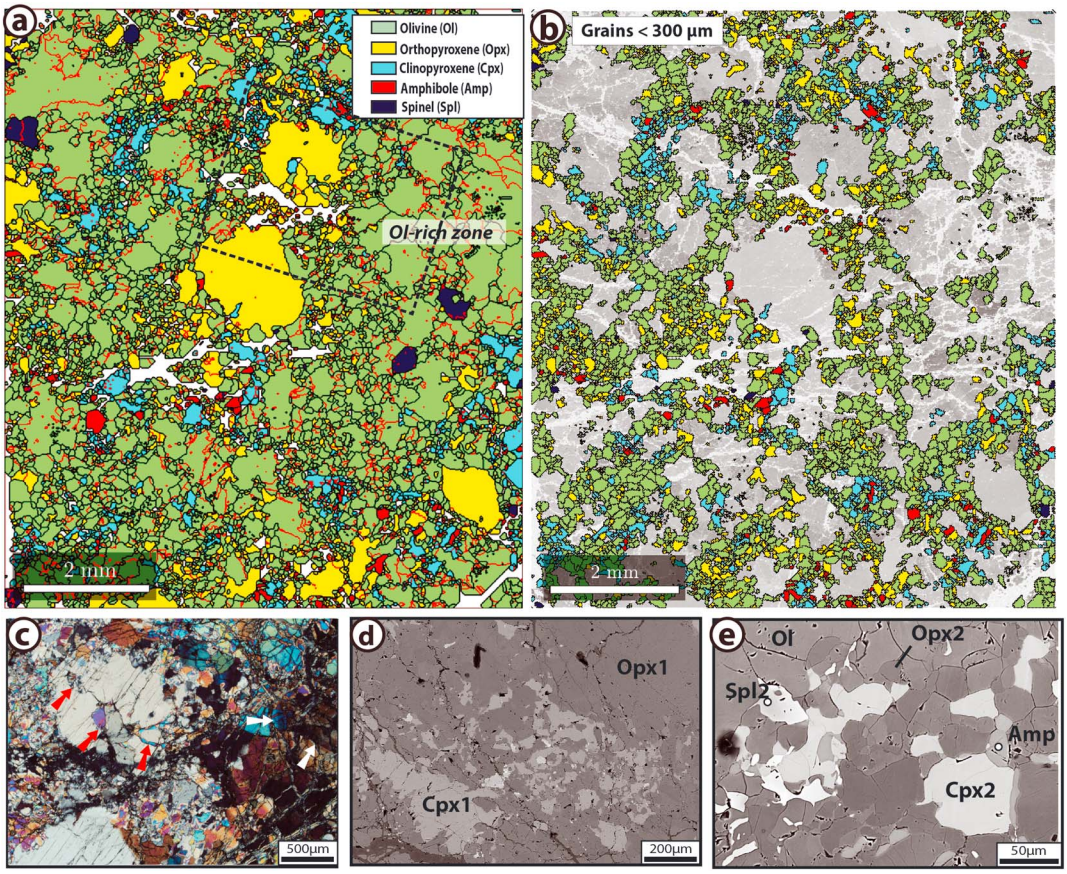

Figure 3. Microstructures and grain textures in protomylonites (a–d: sample SE13-81 and e: sample SE13-83). (a, b) Electron BackScattered Diffraction phase maps (in black: grain boundaries and in red in Figure 3a: subgrain boundaries). In Figure 3b only grains with sizes $<$300 µm are shown on the band contrast image. (c) Microphotograph highlighting the irregular texture of pyroxene porphyroclasts surrounded by the fine-grained polymineralic matrix (location shown in Figure 3a). White arrows point to subgrain walls in large olivine grains and red arrows to fractures dissecting a pyroxene porphyroclast and filled by smaller grains. (d, e) Scanning electron microscope images highlighting the irregular interstitial textures of smaller grained phases (Cpx2, Spl2, Opx2, and Amp). Mineral abbreviations are reported in Figure 3a.

(Figures 3a–3d). Small grains destabilize their grain boundaries and crystallized in fractures dissecting the porphyroclasts in places (Figure 3c). Small grains are, however, also found dispersed as interstitial phases at coarser olivine grain boundaries (Figure 3e). In these finest-grained zones, olivine, orthopyroxene, clinopyroxene, spinel, and amphibole are mixed together. Straight grain boundaries suggest that they are in textural equilibrium (Figures 3b and 3e). EBSD maps reveal that olivine, orthopyroxene, and clinopyroxene minerals from these fine-grained zones may also have subgrain boundaries (Figure 3a).

In mylonites, clinopyroxene and orthopyroxene porphyroclasts may reach aspect ratios of 1:6 with bent exsolution lamella. They are also rounded or have very irregular shapes in places. Olivine grain size ($<$800 µm; Figures 2e and 2f) is more homogeneous than in the less deformed peridotites. In olivine-rich zones, grains are elongated parallel to the foliation, reaching aspect ratios of up to 1:5 (Figure 2c). They share 120° triple junctions in places and may show kink bands subperpendicular to the foliation. In zones where secondary phases are more abundant (Figure 4a), olivine is smaller ($<$200 µm) with very irregular grain boundaries (Figure 4e). EBSD maps show that subgrain boundaries are also present in these olivine grains, as well as in minor phases (Figures 4a and 4e). These minor phases (orthopyroxene, clinopyroxene, spinel, and amphibole) have very irregular interstitial shapes (Figures 4a–4d). They are found at olivine triple grain junctions (Figure 4a), along olivine grain boundaries (forming film-like structures in places) and along olivine subgrain walls near grain boundaries (black zoom in Figure 4a). These phases display cusps in between olivine-olivine grain boundaries (Figures 4b and 4c) and embay (Figure 4d) or completely armor olivine grains in places (Figure 4c).

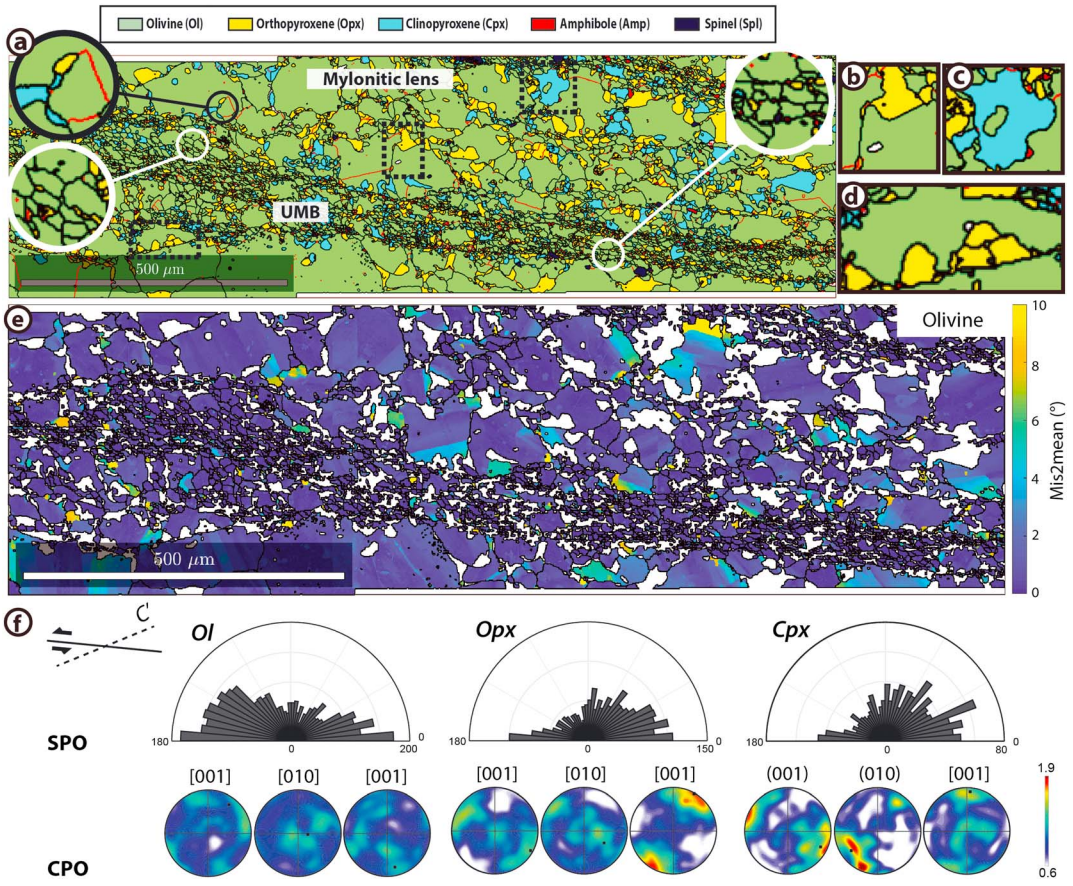

Figure 4. Microstructures and grain textures in a mylonite with ultramylonitic bands (UMB, sample SE13-37A). (a) Phase map and (b, d) selected enlargements (see dashed rectangles for location in Figure 4a). Black lines are grain boundaries and red lines are subgrain boundaries. (e) Olivine grains colored by the intragranular misorientation angle of each pixel compared to the average grain orientation (Mis2mean), showing the presence of subgrain walls in olivine. (f) Shape preferred orientation (SPO) and crystallographic preferred orientation (CPO) distribution of olivine, orthopyroxene, and clinopyroxene in this map. CPO is represented on lower hemisphere pole figures. Black squares indicate the preferred axis orientation (eigenvector E1).

In ultramylonites and UMB, phases are highly mixed (Figure 4a). EBSD maps highlight that olivine and pyroxene may have subgrain boundaries and that olivine quadruple junctions are observable in these zones (white zooms in Figure 4a). These quadruple junctions are filled with olivine, pyroxene, or amphibole grains. In the mylonites and ultramylonites/UMB, minerals have a SPO (Figure 4f). Olivine elongation is close to the shear plane, whereas pyroxene is elongated oblique to it, close to a C'-band orientation.

4.3. Fabric Strength and Boron Isotopic Composition

To characterize the CPO of the different phases, we first quantify their fabric strength and its evolution as a function of grain size reduction, using the M- and J-indexes. The J-index of natural peridotites generally ranges from 1 to 20, with a predominance of values <6 (Tommasi & Vauchez, 2015).

The values of these two indexes are represented in Figures 5a–5c and 5d–5f, respectively, as a function of the mean olivine grain size and peridotite microstructure. J values (from 2.5 to 1.1) indicate that all phases in basal peridotites have weak to very weak CPO (Tommasi & Vauchez, 2015), except for clinopyroxene in one porphyroclastic tectonite (Figure 5f). Olivine fabric strength progressively decreases with decreasing grain size, from porphyroclastic tectonites (M 0.07–0.12 and J 1.8–2.4) to a random fabric in ultramylonites/UMB (M 0.0–0.03 and J 1.1–1.3; Figures 4f, 5a, and 5d). J- and M-indexes of orthopyroxene and clinopyroxene also suggest that their fabric strength slightly decreases from porphyroclastic tectonites to mylonites. However, in contrast to olivine, their CPO strength does not get completely randomized in

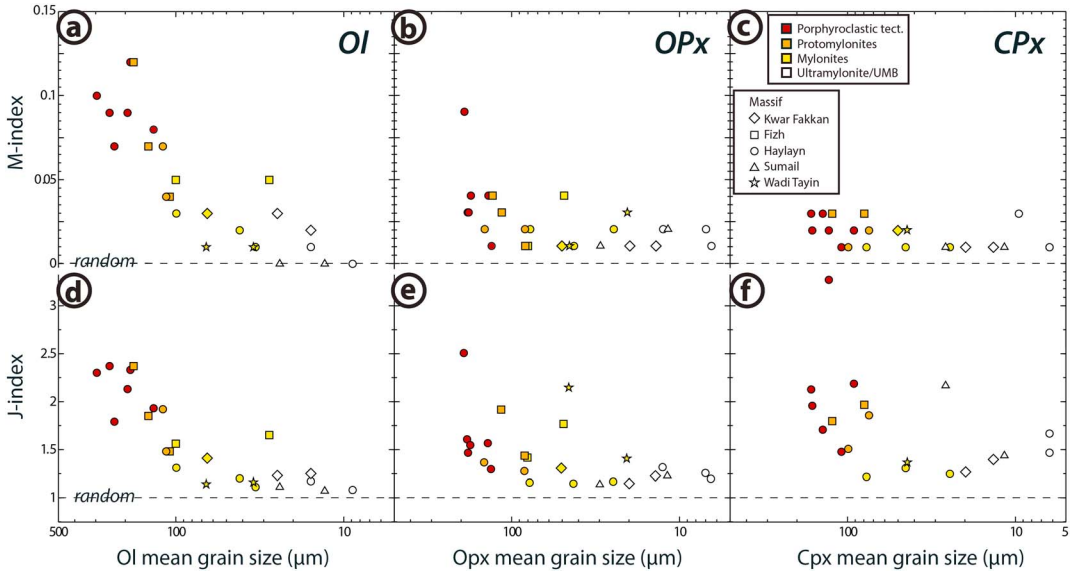

Figure 5. Evolution of crystallographic preferred orientation strength, using the mean grain orientation, for olivine (Ol, left column), orthopyroxene (Opx, middle column), and clinopyroxene (Cpx, right column) as a function of their mean grain size. Values of 0 for the M-index (a–c; Skemer et al., 2005) and 1 for the J-index (d–f; Mainprice & Silver, 1993), indicate that grains are randomly oriented in the sample. See text for further details.

ultramylonite/UMB, remaining weak but present, with that of clinopyroxene potentially getting even stronger than in mylonites (Figures 4f and 5).

We also report the evolution of the boron isotopic composition of the samples taken across the protomylonitic to ultramylonitic shear zone located upsection in the massif of Haylayn, together with constitutive olivine grain size and J-index (Figure 6). The $\delta^{11}B$ of samples reflects their $^{11}B/^{10}B$ ratio, which can be considered as a proxy for fluid-rock interactions (Prigent et al., 2018, and references therein). As noticed above, olivine grain size and J-index decrease from porphyroclastic tectonites to the mylonites (± UMB) located in the core of the shear zone. This decrease in fabric strength is associated with a progressive increase in peridotite $\delta^{11}B$ (i.e., a relative enrichment in ^{11}B compared to ^{10}B) from porphyroclastic tectonites having values (-4 ± 2‰) close to the depleted MORB (Mid-Ocean Ridge Basalt) Mantle (-7.1 ± 0.9‰; Marschall et al., 2017), protomylonites (0 ± 1‰) to mylonites with UMB (+4 ± 1‰).

4.4. Crystallographic Preferred Orientation

To further characterize deformation patterns, we report below the CPO of the different phases. The CPO is shown in Figure S1, and, for the sake of clarity, only eigenvectors corresponding to the preferred axis orientation (E_1) are reported in Figure 7a, on the same pole figure for every sample. On the pole figures, lineation strikes in the east-west direction (*X* axis) and the normal to the foliation points to the north (*Y* axis). For some (proto) mylonitic samples, foliation and lineation were difficult to determine and we thus orientated the sample according to the deformation patterns of nearby ultramylonitic samples.

In all samples, olivine [100] is preferentially aligned in the foliation plane, parallel to the lineation, but gets more dispersed in ultramylonite/UMB (Figures 4f and 7a). Olivine [010] and [001] are either preferentially aligned in the foliation plane, perpendicular to the lineation, orthogonal to the foliation or have a girdle distribution normal to the lineation. In agreement with these observations, we use the fabric-index angle of Michibayashi et al. (2016) to show that olivine mainly displays an E- or D-type fabric in porphyroclastic tectonites; an A-, D-, or E-type fabric in protomylonites; and a D- or E-type fabric in (ultra)mylonites/UMB (which are not randomly oriented; Figure 7b). In the finest-grained zones (Figure 4), olivine has an SPO but a random CPO.

Although orthopyroxene has a weak to very weak CPO (Figure 5), it is generally characterized by a maximum distribution density of [001] axis subparallel to the normal to the foliation plane (Figures 4f and 7a). Axes [100] and [010] are aligned in the foliation plane (showing a clear maximum either subparallel or subperpendicular to the lineation or dispersed along a girdle within this plane).

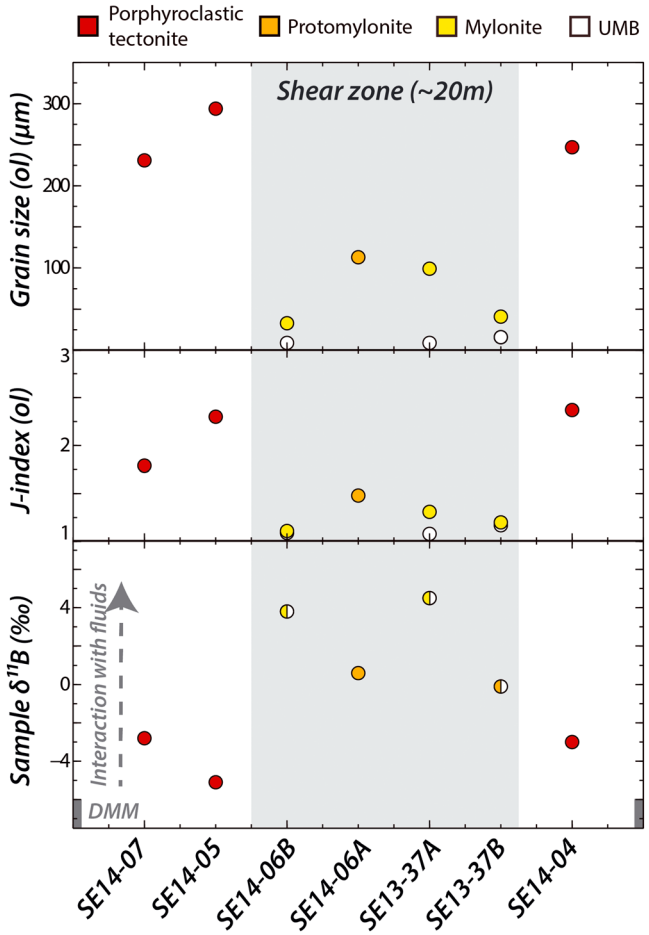

Figure 6. Evolution of olivine (Ol) grain size, crystallographic preferred orientation strength (characterized by the J-index) and sample $\delta^{11}B$ along one protomylonitic to ultramylonitic shear zone located in the Haylayn massif, ~170 m away from the basal contact. Gray, vertical bands on the lowermost diagram recall $\delta^{11}B$ values of the depleted MORB mantle (Marschall et al., 2017). Gray vertical overlay: shear zone location. DMM = depleted MORB mantle.

Clinopyroxene CPO is more dispersed and thus hard to describe in detail (Figures S1 and 7a). It is, however, noticeable that, as orthopyroxene, clinopyroxene [001] axis, which is also its main Burgers vector being thus generally located subparallel to the lineation (Naze et al., 1987; Steuten & Van Roermund, 1989; Van Roermund & Boland, 1981), is oblique to the foliation and even normal to it in the majority of analyzed samples (Figures 4f and 7a). In the more deformed rocks, mylonites, ultramylonites/UMB and some protomylonites, orthopyroxene, and clinopyroxene [001] axes are located close (<30°) to each other (Figure 7c). Figure 4 shows that the orientation of the pyroxene [001] long axes is close to their direction of elongation (SPO) and to a C′-band orientation.

4.5. Misorientation Rotation Axes

Rotation axes accommodating the low angle (2–10°) misorientations within a crystal may allow identification of its dominant active slip system(s). The main low-angle misorientation (LAM) rotation axis (or axes) is (are) identified from inverse pole figures in Figure S1, and examples of the different types of LAM distribution are reported in Figures 7d–7f. Low-angle misorientations within olivine grains are mainly accommodated by rotation around their [010] axis (Figure 7d). This is consistent with the dominant activation of the olivine (001)[100] slip system, hence with the predominance of olivine with E-type CPO (Figures 7a and 7b). However, in a few (proto)mylonites and ultramylonites, rotation around the [001] olivine axis is equally frequent, even slightly dominant (SE14-06B; Figure S1), suggesting that the (010)[100] is also significantly activated in these samples. In the finest-grained ultramylonite/UMB, misorientation axes are more dispersed, maybe due to lesser amount of intragranular misorientations in the grains (Figure S1).

For orthopyroxene, the main rotation axis is also [010] but rotation around [001] is dominant in a few (ultra)mylonitic samples (Figure 7e). Misorientation rotation axes for clinopyroxene are strongly dispersed and ambiguous (Figure S1), with only weak maxima close to [001], mostly in porphyroclastic tectonites and (proto)mylonites (Figure 7f).

5. Discussion

The above results confirm that grain size reduction occurred during continuous ductile deformation and cooling of the basal banded unit of the Semail ophiolite. Progressive strain localization into narrower shear zones results in the preservation of peridotites equilibrated at different stages of deformation and cooling, from porphyroclastic tectonites (~1200 °C), (proto)mylonites (~900–800 °C) to ultramylonites/UMB (~700 °C). The following discussion focuses on the mechanism(s) responsible for this evolution.

5.1. Deformation in Porphyroclastic Tectonites

Preserved porphyroclastic tectonites from the Haylayn massif (spinel lherzolites and Cpx-harzburgites) indicate that significant amounts of clinopyroxene were present before lower temperature ductile deformation. Olivine in these rocks display E- and D-type CPOs (Figure 7b) and dominant LAM rotation axes around the [010] axis (Figure 7d). Olivine E- and D-type CPOs suggest activation of the (001)[100] and (0kl)[100] dislocation slip systems. Preferential activation of the (001)[100] slip system in olivine has been reported in experiments at moderate water content (200–1000 H/10^6Si), low stresses (400 MPa), $P < 2.2$ GPa, and solidus to hypersolidus temperature (Katayama et al., 2004). In natural mantle shear zones, it has also been described at subsolidus conditions and has been attributed to deformation (1) under hydrous conditions (Cao et al.,

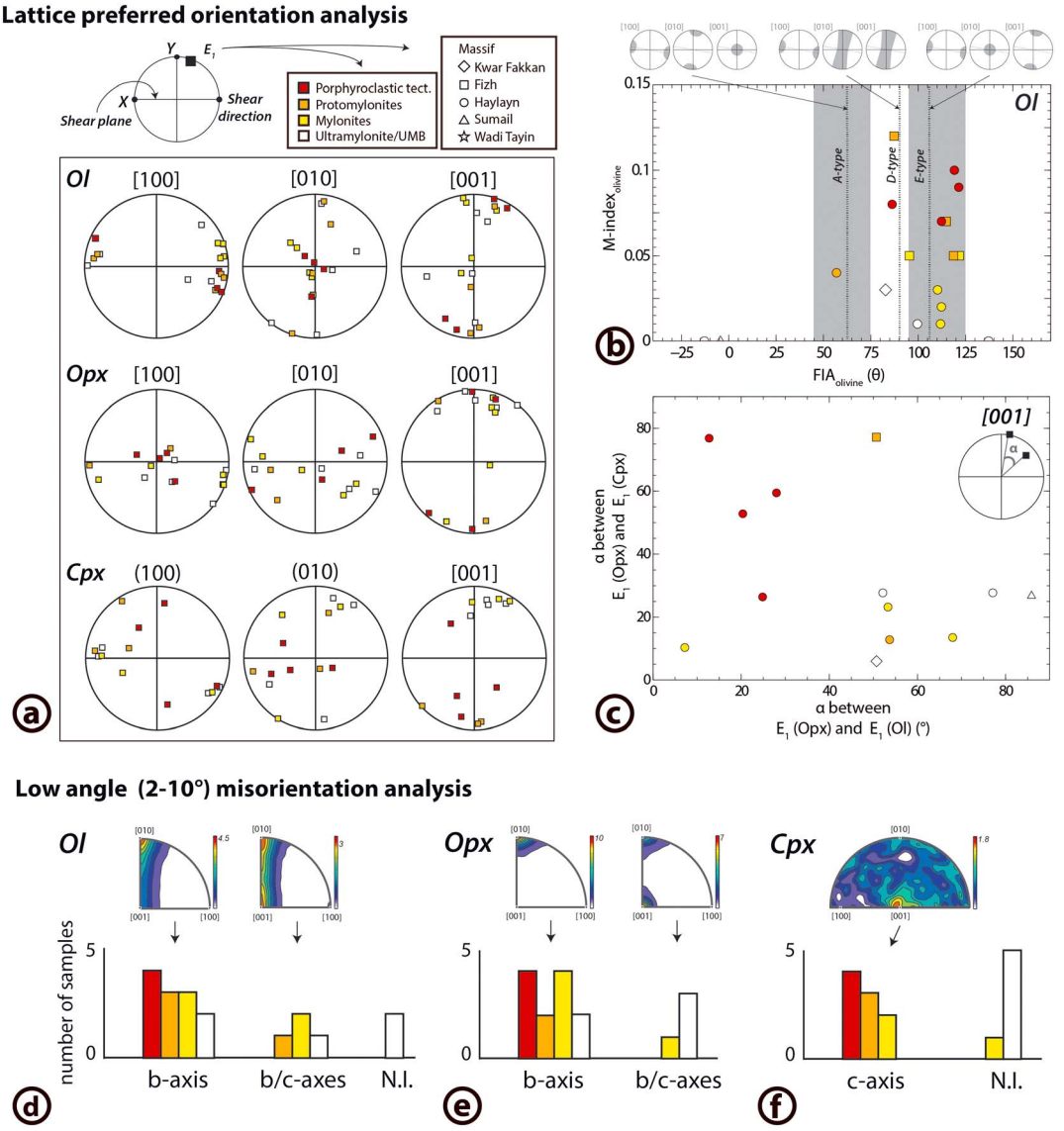

Figure 7. (a–c) Analysis of olivine (Ol), orthopyroxene (Opx), and clinopyroxene (Cpx) crystal preferred orientations (CPO). CPO is projected on lower hemisphere equal area stereograms: the *X* axis represents the lineation and the *Y* axis the normal to the sample foliation. CPOs (reported in Figure S1) are computed considering one value per grain only. (a) In pole figures only the preferred orientation of each mineral crystallographic axis (eigenvector E_1) is represented for each analyzed sample. (b) Olivine fabric-index angle (FIA) of Michibayashi et al. (2016) as a function of olivine fabric strength (M-index; cf Figure 5). The FIA allows identification of olivine fabric types. Gray fields are from Michibayashi et al. (2016). (b) Angle between E_1 of Opx and Ol [001] axes as a function of the angle between E_1 of Opx and Cpx [001] axes on the *XY* plane. (d–f) Main rotation axis (or axes) of intragranular misorientations inferred from the analysis of inverse pole figures of low-angle misorientation distributions (cf. Figure S1). The *b* and *c* axes for samples showing a clear maximum around one of these axes and *b*/*c* axes for samples showing two maxima around both *b* and *c* axes (N.I. when the distribution is too dispersed to clearly identify the rotation axis). Examples of inverse pole figure are shown above (samples SE14-05, SE14-06A for *b*/*c* axes for Ol and SE13-113 for *b*/*c* axes for Opx). Color coding and symbols (a–c) are for sample microstructure and massif, respectively.

2015; Harigane et al., 2013; Hidas et al., 2016; Jung et al., 2014; Mehl et al., 2003; Michibayashi et al., 2009; Michibayashi & Oohara, 2013) or (2) in the presence of melt (Suhr, 1993; Tommasi et al., 2006). The E-type olivine CPO in the protolith may therefore be due to a mantle containing moderate amount of water or affected by melt/rock interaction processes at 1200 °C before LT deformation. The second hypothesis may better explain the observed relatively low mineral CPO strength and mean grain sizes (Figures 2d and 5), as melt-assisted precipitation can produce new, smaller, and less oriented phases.

5.2. Deformation in Protomylonites to Ultramylonites: Evidence for Fluid-Assisted Grain Size Reduction

5.2.1. Olivine Deformation Mechanisms

The progressive grain size reduction from protomylonites to ultramylonites/UMB (Figure 2d) is an ubiquitous process observed in mantle ductile shear zones during increasing deformation and strain localization (Boullier & Gueguen, 1975; Drury et al., 1991; Tommasi & Vauchez, 2015; Warren & Hirth, 2006). As in similar mylonitic shear zones, our observations suggest that this process of grain size reduction is associated with a progressive transition in olivine deformation mechanism from dislocation creep to grain size sensitive (GSS) creep. Indeed, undulose extinction and the presence of subgrains in olivine in (proto)mylonites to ultramylonites/UMB (Figures 2, 3, and 4), as well as the occurrence of triple junctions between olivine grains, suggest that they deformed through dislocation creep. Moreover, olivine CPO geometry is consistent with the movement of dislocations inferred from the analysis of the LAMs. Olivine with A-type fabrics shows equally frequent rotation of their dislocations around the [001] and [010] axes, whereas olivine with D-type and E-type fabrics display mostly rotation around the [010] axis. This suggests that olivine CPO developed by dislocation creep, by the dominant activation of the (010)[100], and the (001)[100] slip systems, respectively. The progressive decrease in olivine CPO strength with decreasing grain size (Figure 5), a correlation also observed by Ambrose et al. (2018) in the basal part of the mantle in the Kwar Fakkan massif, therefore indicates a decreasing contribution of dislocation creep to olivine deformation during shearing. In ultramylonites and UMB, the very fine grain sizes and CPO randomization of olivine imply that olivine deformation no longer dominantly occurs by dislocation creep but rather by a GSS creep process. In these zones, olivine has a SPO subparallel to the shear plane, indicating a significant contribution of diffusion creep, and also shares quadruple grain boundary junctions, suggesting that the GSS process of grain boundary sliding (GBS) might have also been active.

Such a transition in olivine deformation mechanism from dislocation creep to GSS creep is an efficient weakening mechanism (Braun et al., 1999; Drury et al., 1991; Karato & Wu, 1993; Newman et al., 1999; Précigout & Gueydan, 2009; Vissers et al., 1995; J. M. Warren & Hirth, 2006), enabling strain localization in the ductile mantle. As in those studies, we observe that grain size reduction is associated with a phase mixing process. As noted by Ambrose et al. (2018), this phase mixing process and the increase of minor phases observed in ultramylonites/UMB likely inhibited olivine grain growth and pinned olivine grain size in the GSS creep domain (e.g., Evans et al., 2001). Grain sizes of basal peridotites indeed follow a Zener pinning relationship (Figure S2; e.g., Hansen & Warren, 2015; Herwegh et al., 2011; Tasaka & Hiraga, 2013; Tasaka et al., 2014). However, in contrast to Ambrose et al. (2018), we show that grain size reduction in (proto)mylonites is not associated with an increase in minor phase proportion (Figure 2e). This indicates that the initial olivine grain size reduction, and so peridotite weakening, is not a direct consequence of initial differences in minor phase abundance.

5.2.2. Mechanism (s) of Grain Size Reduction and Phase Mixing

Different mechanisms have been invoked to account for these combined processes of grain size reduction and phase mixing in ductile mantle shear zones: dislocation-mediated dynamic recrystallization and GBS-related grain switching events (e.g., Linckens et al., 2014), dynamic recrystallization and stress-induced differential cation diffusion (Tasaka et al., 2017), or dispersed nucleation of fine grains through dissolution-precipitation processes (Hidas et al., 2016; Précigout et al., 2017; Précigout & Stünitz, 2016), associated with metamorphic reactions (De Ronde & Stünitz, 2007; De Ronde et al., 2005; Newman et al., 1999; Toy et al., 2010; Vissers et al., 1995) or melt-rock interaction (Dijkstra et al., 2002; Kaczmarek & Tommasi, 2011). The evidence for dislocation mobility in olivine and pyroxene (undulose extinctions and subgrain walls; Figures 3 and 4) and the occurrence of olivine triple junctions suggest that dynamic recrystallization by subgrain rotation partly contributed to reducing grain size. The possible activation of olivine GBS (see above) in fine-grained zones might have played a role in mixing phases. The following textural and microstructural observations, however, suggest that grain size reduction and phase mixing were principally triggered by dissolution/precipitation processes, whereby finer grains precipitated dispersedly, and grew, at the expense of coarser grains.

1. Drastic grain size reduction within protomylonites (from millimetric to $<$300 μm grains) is mainly observed around pyroxene porphyroclasts, through crystallization of a finer-grained polymineralic matrix, in which olivine, clinopyroxene, spinel, amphibole, and orthopyroxene are mixed and in textural

equilibrium (Figures 3a–3c). The polymineralic nature of these finer-grained zones can hardly be explained by dynamic recrystallization of porphyroclasts only (e.g., Linckens et al., 2015).

2. From protomylonites to ultramylonites/UMB, coarser grains have very irregular grain boundaries due to embayment of finer grains (Figures 3a–3c and 4e) and fracture-like features filled by finer grains (Figure 3c). In protomylonites, some porphyroclasts are almost completely replaced by these fine-grained mixture and smaller grains have interstitial textures (Figures 3d and 3e). In ultramylonite/UMB, these phases are found dispersed in the olivine matrix at olivine triple/quadruple grain junctions, along olivine grain boundaries (forming film-like structures in places, embaying and/or armoring olivine grains), and olivine subgrain walls near grain boundaries (Figures 4a–4d). Such interstitial textures of secondary minerals, already observed in mantle (Hidas et al., 2016) and crustal rocks (e.g., Fusseis et al., 2009; Kilian et al., 2011), are generally interpreted as evidencing crystallization by mineral precipitation and subsequent growth at the expense of the matrix minerals, mainly olivine here.
3. In contrast to olivine, the (overall very weak) CPO strength of small pyroxene grains does not progressively decrease during ongoing deformation (Figure 5) and does not get randomized in ultramylonites/UMB (Figures 4f and 5). Moreover, while the dominant LAM rotation axis in orthopyroxene ([010]; Figure 7e) and in clinopyroxene ([001]; Figure 7f) is consistent with former studies (Achenbach et al., 2011; Kaczmarek & Tommasi, 2011; Soustelle et al., 2010), their CPO geometry is incompatible with any known dislocation slip system. Indeed, the [001] axis corresponds to the Burgers vector in pyroxene (e.g., Bascou et al., 2002; Naze et al., 1987; Van Roermund & Boland, 1981; Zhang et al., 2006) and should therefore be observed subparallel to the lineation as in the majority of peridotitic natural shear zones (Achenbach et al., 2011; Kaczmarek & Tommasi, 2011; Soustelle et al., 2010). In contrast, the [001] axis of both orthopyroxene and clinopyroxene is systematically (Figure 7a), and consistently (Figure 7c), oblique to the foliation plane and even normal to it in most cases. All these combined arguments support that the CPO of pyroxene does not result from the movement of intracrystalline dislocations.
4. Such a CPO geometry of pyroxene has been reported in a few deformed peridotites and attributed to pyroxene syntectonic, oriented precipitation, and growth (Dijkstra et al., 2002; Hidas et al., 2016; Suhr, 1993). The overall weak CPO of pyroxene, which does not get randomized during deformation, and the orientation of their long crystallographic axis ([001]) subparallel to the direction of their SPO and to a C′-band orientation (Figure 4f) support this interpretation. Moreover, the fact that the directions of pyroxene elongation and [001] axis are at very high angle to olivine SPO direction and to σ_3 strongly suggests that precipitation and growth of fine-grained minerals occurred mainly along grain boundaries that were under deviatoric tension. The presence of tiny grains at olivine quadruple junctions hints that GBS-induced cavities might also have been the locus of new mineral precipitation.

These arguments therefore support that dissolution/precipitation processes were key in promoting the initial drastic grain size reduction in protomylonites and progressive grain size reduction and phase mixing from protomylonites to ultramylonites/UMB.

5.2.3. Fluid-Assisted Deformation and Fluid Focusing in Shear Zones

Crystallization of amphibole in equilibrium with other phases in the finer-grained polymineralic zones (Figures 3 and 4) testifies to the presence of hydrous fluids during deformation and dissolution/precipitation processes. This is also confirmed by chemical data that show strong enrichments of fine-grained minerals in (proto)mylonites in fluid mobile elements (especially boron; Prigent et al., 2018). This observation is also in agreement with the predominant activation of olivine (001)[100] dislocation slip systems in (proto)mylonites to ultramylonite/UMB (Figure 7), which is generally activated in hydrous conditions (Cao et al., 2015; Harigane et al., 2013; Hidas et al., 2016; Jung et al., 2014; Katayama et al., 2004; Mehl et al., 2003; Michibayashi & Oohara, 2013; Précigout et al., 2017). The geochemistry of newly crystallized fine grains and whole rock isotopic compositions indicate that these aqueous fluids bear a subduction signature (Khedr et al., 2014; Prigent et al., 2018; Yoshikawa et al., 2015). These authors proposed that these fluids were most likely derived from metamorphic sole dehydration (Ishikawa et al., 2005) and fluid migration through the above mantle wedge (i.e., the banded unit). Dissolution-precipitation processes consistently occurred in (proto)mylonites at temperatures matching those of the amphibolitic to granulitic HT sole metamorphic peak (i.e., ~900–800 °C; Figure 1a). We therefore evidence that the release of subduction fluids through the hot plate interface and subsequent fluid/peridotite interaction triggered dissolution/precipitation processes and intense grain size reduction in the above mantle, forming the basal

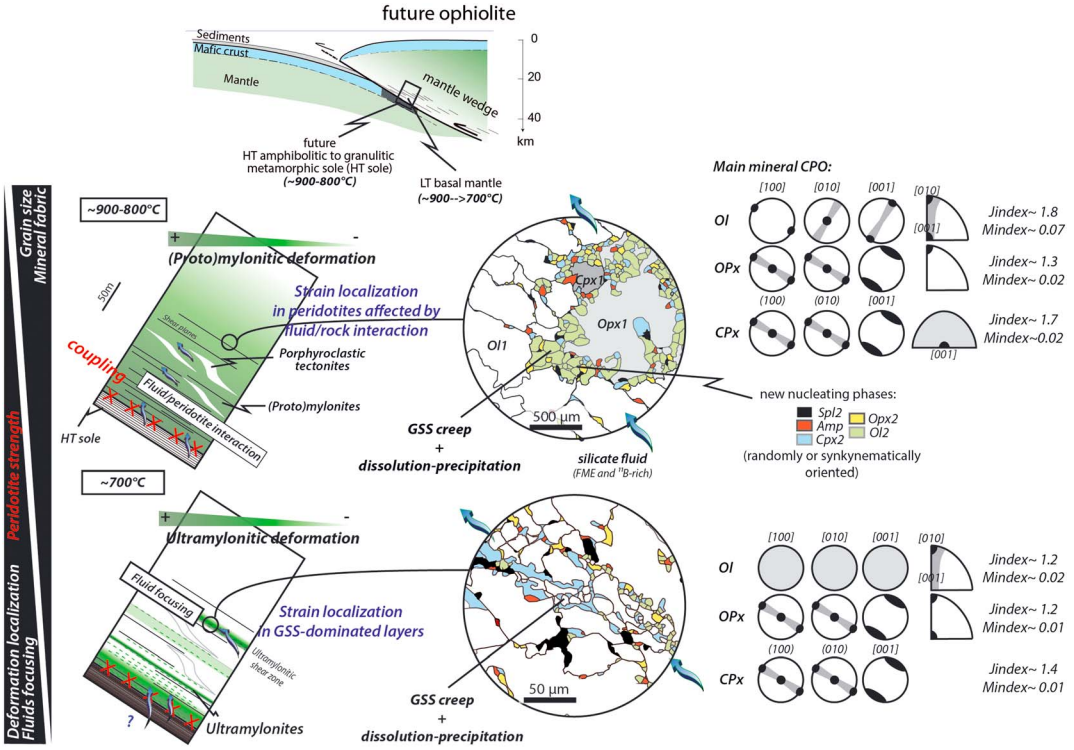

Figure 8. Summary of petrological and microstructural changes observed in the banded unit peridotites during LT deformation, from (proto)mylonites at 850–750 °C to ultramylonites at 750–650 °C. This two-step evolution is set back within the geodynamic setting of subduction initiation, HT sole, and banded unit (de)formation. Fluids derived from the metamorphosing HT sole percolated through the present-day banded unit at ~850 °C, inducing fluid/peridotite interaction and crystallization of new smaller phases. Similar fluid/peridotite reactions prevailed during the ultramylonitic stage, further reducing aggregate grain size. LT = low temperature; HT = high temperature; CPO = crystallographic preferred orientation; GSS = grain size sensitive.

(proto)mylonites. The presence of interstitial hydrous fluids likely enhanced mass transfer at grain boundaries (e.g., Demouchy et al., 2012) and thus dissolution/precipitation processes and grain size reduction during ongoing shearing.

In addition, boron isotopic analyses from the Haylayn shear zone (Figure 6) indicate that grain size and fabric strength reduction (from porphyroclastic tectonites, protomylonites to UMB-bearing mylonites) is associated with a progressive increase in sample $\delta^{11}B$ values (i.e., $^{11}B/^{10}B$ ratios) from near-depleted MORB mantle values (Marschall et al., 2017) to +4‰ (Figure 7). Since ^{11}B is preferentially mobilized in fluids relative to ^{10}B, this increase in peridotite $\delta^{11}B$ values reflects (1) focusing of fluids in LT shear zones (preserving lenses of porphyroclastic tectonites) and (2) higher interaction of peridotitic minerals with fluids in mylonites compared to protomylonites. This suggests that fluid migration through the mantle was not totally pervasive but focused along actively deforming shear zones running parallel to the plate interface.

5.3. Fluid/Rock Interactions During Deformation and Progressive Strain Localization

5.3.1. Mechanisms of Strain Localization and Fluid Migration in a Cooling Mantle Wedge

Our observations suggest that fluid/rock interactions strongly influenced the deformation of the basal peridotites by enhancing grain size reduction from protomylonites to (ultra)mylonites (i.e., from ~900 to 700 °C) and that, in turn, deformation focused fluid migration.

In (proto)mylonites, subduction fluid/peridotite interaction led to a drastic grain size reduction by dissolution of millimetric grains and precipitation of polymineralic aggregates composed of grains <300 µm (Figure 8). This grain size is small enough in the conditions of banded unit deformation (Ambrose et al., 2018) to trigger a switch in the dominant deformation mechanism from dislocation to wet diffusion creep of olivine. This fluid-induced change in olivine dominant deformation provides an efficient weakening

mechanism, enabling strain localization in the 200- to 500-m-thick banded unit at 900–800 °C (Braun et al., 1999; Drury et al., 1991; Karato & Wu, 1993; Newman et al., 1999; Précigout & Gueydan, 2009; Vissers et al., 1995; Warren & Hirth, 2006), that is, in (proto)mylonites produced by interaction with the subduction fluids compared to less deformed (dry) porphyroclastic tectonites lenses and overlying peridotites (Figure 8). More extensive fluid/peridotite interaction in mylonites than in protomylonites, as highlighted by B isotopes (Figure 5), explains variations in mantle deformation above the interface at this tectonic stage.

Ultramylonitic shear zones within the banded unit indicate further grain size reduction and strain localization in narrower shear zones at ~700 °C, as peridotites were deforming through GSS creep (Figure 8). This suggests that continuous dissolution/precipitation processes, and nucleation-induced grain size reduction, phase mixing, and grain boundary pinning, further forced strain to localize in narrow ultramylonitic shear zones.

Heterogeneous deformation within the banded unit, reflecting heterogeneous fluid circulation and focusing in actively deforming peridotites, suggests, in turn, that ductile deformation of the mantle wedge also influenced subduction fluid circulation by channelizing them toward active shear zones running parallel to the plate interface. Fluid pumping implies permeability changes with increasing deformation and/or pressure gradients for moving fluids. Explanations may include (1) initial heterogeneous fluid distribution and pressure gradients between strong (fluid poor) and weak (fluid rich) domains (Holtzman et al., 2003; Kelemen & Dick, 1995; Stevenson, 1989; Tommasi et al., 1994), (2) progressive grain size reduction enhancing rock permeability (Soustelle et al., 2010; Wark & Watson, 2000), or (3) increase of GBS contribution during deformation due to grain size reduction, a deformation mechanism that may increase rock dynamic porosity by promoting cavitation (Fusseis et al., 2009; Mancktelow et al., 1998; Menegon et al., 2015; Précigout et al., 2017; Rybacki et al., 2008). In ultramylonites, the presence of nucleated phases at quadruple olivine grain boundaries (Figure 4a) and the increase in the abundance of minor phases (Figure 2e) may support that GBS has played a role in promoting rock porosity but more work should be done to study the exact driving mechanism. Whatever the exact mechanism, the feedbacks between fluid migration and peridotite deformation documented here for a young (incipient) mantle wedge are key to understand fluid (and/or melt) transport in active subduction zones and the distribution of water across such hot subduction interfaces.

5.3.2. Progressive Deformation of the Basal Banded Unit: Mechanical Coupling and Exhumation Processes Along the Subduction Interface

Progressive deformation of the banded peridotites can be set back within the broader picture of subduction infancy. The (proto)mylonitic deformation took place at ~900–800 °C, while the underlying HT sole was (de)forming and dehydrating at ~ 30 km depth. Based on the worldwide observation that banded peridotites and HT soles get juxtaposed at ~850 °C and 1 GPa, Agard et al. (2016) concluded that ultramafic and mafic protoliths must have comparable mechanical strength at these conditions and that this process controls the shift from a mechanically decoupled to coupled plate interface, which is required to scrap off metamorphic soles at these specific conditions. Comparison of the rheology of basalts (HT sole) with that of wet peridotites (present-day banded unit, i.e., the mantle wedge) suggests that the switch from olivine deformation by dislocation creep to wet diffusion creep in (proto)mylonites, as a result of extensive fluid/rock interaction, leads to similar effective viscosities of ~10^{20} Pa s for the HT sole and the banded unit (Agard et al., 2016). We therefore propose that the observed dramatic grain size reduction induced by subduction fluid/peridotite interaction at the (proto)mylonitic stage is responsible for mantle wedge weakening and mechanical coupling between the downgoing slab crust and the mantle of the future Semail ophiolite (Figure 9a).

The decompression recorded in the HT sole, from its formation/accretion at ~1 GPa to its emplacement on top of the LT sole at ~0.5 GPa, suggests that both units (banded unit and HT sole) were exhumed together from ~30 to ~15 km along the subduction interface before emplacement onto the LT sole (and before the final emplacement of the ophiolite). Ultramylonitic shear bands must therefore have developed during this exhumation stage (Figure 9b). Future studies should help to elucidate the driving mechanism for this exhumation (inset in Figure 9b), which could tentatively be due to (i) shearing and exhumation of the banded unit (and HT sole) with respect to the overlying mantle, probably along ultramylonitic zones and/or (ii) thinning within the overlying ductile mantle wedge (for a large part within the banded peridotites) resulting in the

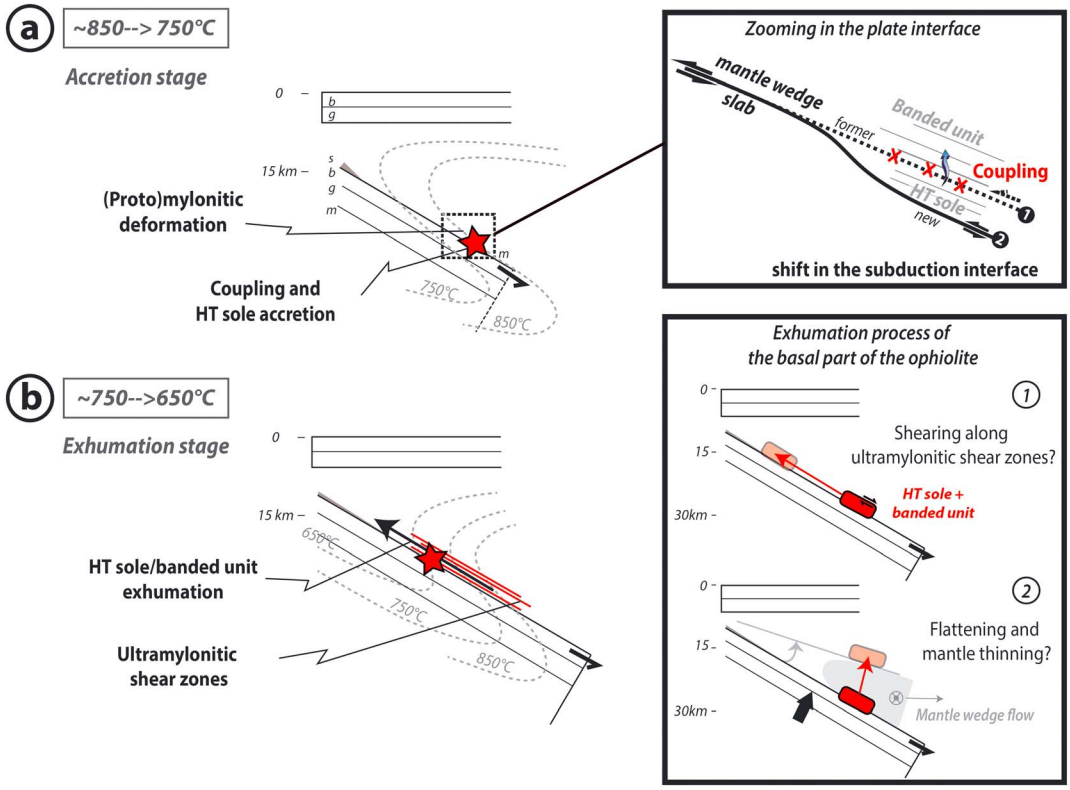

Figure 9. Importance of the reported deformation mechanisms for the geodynamic evolution. (a) At 850–750 °C, (proto) mylonites weakening due to the interaction between banded unit peridotites and fluids released at ~30 km by the HT metamorphic sole triggered plate interface coupling and ensuing accretion of the HT sole (i.e., by shifting the subduction interface within the slab). (b) At 750–650 °C, ultramylonitic deformation accompanies the joint exhumation of the HT sole and the banded unit along the interface, until their accretion on top of the LT sole at ~15 km. Although the exact driving mechanism for their exhumation is unknown, two hypotheses are featured: shearing along ultramylonitic shear zones (inset 1) and subduction flattening and mantle thinning (inset 2). HT = high temperature; LT = low temperature.

observed pressure decrease and *passive* exhumation of the two basal units. For the second scenario, it would be essential to characterize the amount of deformation and thinning along ultramylonitic shear bands. The first scenario would imply that, during the ultramylonitic stage (Figure 9b), deformation and fluid migration across the banded peridotites may relate at least in part to exhumation processes and not solely to subduction-related processes.

5.4. Implications for Active Subduction Zones

Regenauer-Lieb et al. (2001) showed that subduction (and therefore plate tectonics) relies on the progressive release of water by the subducting plate while sinking. Their numerical results suggest that this process triggers a weakening of the mantle wedge which, combined to shear heating, is needed to create a narrow shear zone at the plate interface during subduction infancy, allowing for subduction to proceed. Here we show that mantle wedge weakening due to peridotite interaction with subduction fluids at 900–800 °C (without any evidence of shear heating) led to coupling of the plate interface and localization of the high stress deformation in a narrow (<1 km) shear zone (200- to 500-m banded unit and ~100-m HT sole). Inferred viscosity for this shear zone is around 10^{20} Pa s (Agard et al., 2016; Ambrose et al., 2018; Linckens, Herwegh, Müntener, & Mercolli, 2011; Tasaka et al., 2014), consistent with the low viscosity required in numerical models (Regenauer-Lieb et al., 2001). We also show that this process of high strain localization is achieved due to intense fluid/peridotite interaction processes and focusing of subduction fluids in mantle wedge shear zones running parallel to the plate interface. Feedback processes between fluid percolation and strain localization limit fluid migration to shallower levels of the mantle wedge (Prigent et al., 2018), thus producing a narrow fault-like plate interface in the ductile deformation regime.

The observed coupling between the ductile mantle wedge (~900–800 °C) and the downgoing plate at ~1 GPa is likely to take place in active hot subduction zones as rheologies should be similar and perhaps more generally near subarc depths. Thermal models indeed predict that such ductile mantle wedge (i.e., with similar temperatures) is in contact with eclogites at subarc depths in mature subduction zones (Abers et al., 2017; Syracuse et al., 2010). The increase of pressure is not expected to greatly influence the deformation mechanisms of ductile peridotites (and therefore all the observed feedback processes between deformation, fluid migration, and strain localization) but to increase their ductile strength (Hirth & Kohlstedt, 2003). It would be therefore important to compare this increase in peridotite strength with that of the downgoing plate (from amphibolite to eclogite rheology) to discuss the models supporting that, at these depths, the subduction interface is coupled (Arcay et al., 2007; van Keken et al., 2002; Wada & Wang, 2009). To do so, this study points out the importance of subduction fluid/peridotite interaction processes and the need for constraining the rheological laws for hydrated polymineralic peridotites at subsolidus temperatures, including the effect of hydrous fluid present at grain boundaries and promoting grain size reduction through dissolution-precipitation processes.

Our results also show that interaction of mantle wedge ductile peridotites with fluids is associated with (1) grain size reduction, (2) activation of olivine (001)[100] slip system, and (3) the oriented precipitation of new minerals leading to phase mixing and drastic reduction of mineral CPO strength. All these processes should have major consequences on the seismic signature of this deep part of the hydrated mantle wedge, drastically decreasing wave velocities and anisotropy (Tommasi & Vauchez, 2015). Constraining the exact physical properties of these peridotites appears therefore important for refining and interpreting tomographic models of subduction zones.

6. Conclusions

Detailed petrological and microstructural SEM/EBSD observations allowed us to characterize the evolution of grain size and deformation mechanisms in the basal banded unit peridotites from the Semail ophiolite. These rocks, located immediately above the plate interface during subduction infancy, experienced fluid-assisted progressive ductile deformation during their protomylonitic to ultramylonitic deformation, from ~900–800 down to ~700 °C.

Reaction of peridotites with subduction fluids from ~900 to 800 °C led to a drastic grain size reduction through the dissolution of coarser millimetric grains and precipitation of new, smaller ($<$300 μm), and synkinematically oriented grains leading to the formation of (proto)mylonites. These processes account for the observed (1) polymineralic nature of the fine-grained zones, (2) interstitial textures and mixing of small grains, (3) (very) weak CPO of all minerals, and (4) pyroxene CPO geometry. This grain size reduction assisted by fluid-peridotite interaction led to a rapid switch in olivine deformation from dislocation to GSS creep. This decreased the strength of the banded unit peridotites significantly and, at the subduction scale, controlled the shift from a mechanically decoupled to coupled plate interface during detachment/underplating of the HT metamorphic sole beneath the banded peridotites. Release of subduction fluids by the downgoing plate and subsequent fluid/mantle interaction processes appears therefore as key processes that control mantle wedge rheology and plate interface regime at short time scales.

At ~700 °C, continuous nucleation of smaller grains during ongoing deformation (combined with dislocation creep-related dynamically recrystallization) led to further reduction of aggregate grain sizes and mineral CPO strength in the GSS creep domain of olivine deformation. Development of these ultramylonitic shear zones can be ascribed to the coeval exhumation of the banded unit peridotites and HT sole along the plate interface.

Results hint at increasing fluid focusing in actively deforming peridotites, advocating for nonpervasive fluid/peridotite interactions and feedback mechanisms between ductile deformation and fluid migration. This focusing of fluid along mantle shear zones developing parallel to the plate interface has contributed to localize the high stress deformation within a narrow ($<$1 km) shear zone along this ductile portion of the plate interface.

Similar mechanisms may prevail in mature (cooler) subduction zones at higher pressure and control plate interface mechanical coupling at subarc depths.

Acknowledgments
We warmly thank F. Barou for his support and expertise on SEM-EBSD techniques, to D. Delmas and C. Nevado for preparing high-quality thin sections, and to A. Tommasi for helpful discussions. We would also like to thank D. Lemarchand and M. Ulrich for their help in the acquisition of B isotopic data and B. Dubacq, A. Chauvet, A. Plunder, M. Soret, and P. Yamato for their contribution during fieldwork. This manuscript benefited from constructive comments from two anonymous reviewers and the Journal Editor M. Walter. This project was funded by the Agence Nationale de la Recherche We warmly thank F. Barou for his de France (I. U. F. to P. A.) and the Labex OSUG@2020 (ANR10 LABX56). Microstructural data from the EBSD maps used in this study are reported in Table 1. Boron geochemical data are listed and discussed in more details in Prigent et al. (2018).

References

Abers, G. A., van Keken, P. E., & Hacker, B. R. (2017). The cold and relatively dry nature of mantle forearcs in subduction zones. *Nature Geoscience*, *10*(5), 333–337. https://doi.org/10.1038/ngeo2922

Abramson, E. H., Brown, J. M., Slutsky, L. J., & Zaug, J. (1997). The elastic constants of San Carlos olivine to 17 GPa. *Journal of Geophysical Research*, *10,2*(B6), 12,253–12,263. https://doi.org/10.1029/97JB00682

Achenbach, K. L., Cheadle, M. J., Faul, U., Kelemen, P., & Swapp, S. (2011). Lattice-preferred orientation and microstructure of peridotites from ODP Hole 1274A (15 39′ N), mid-Atlantic ridge: Testing models of mantle upwelling and tectonic exhumation. *Earth and Planetary Science Letters*, *301*(1-2), 199–212. https://doi.org/10.1016/j.epsl.2010.10.041

Agard, P., Jolivet, L., Vrielynck, B., Burov, E., & Monie, P. (2007). Plate acceleration: The obduction trigger? *Earth and Planetary Science Letters*, *258*(3-4), 428–441. https://doi.org/10.1016/j.epsl.2007.04.002

Agard, P., Yamato, P., Soret, M., Prigent, C., Guillot, S., Plunder, A., et al. (2016). Plate interface rheological switches during subduction infancy: Control on slab penetration and metamorphic sole formation. *Earth and Planetary Science Letters*, *451*, 208–220. https://doi.org/10.1016/j.epsl.2016.06.054

Ambrose, T. K., Wallis, D., Hansen, L. N., Waters, D. J., & Searle, M. P. (2018). Controls on the rheological properties of peridotite at a palaeo-subduction interface: A transect across the base of the Oman–UAE ophiolite. *Earth and Planetary Science Letters*, *491*, 193–206. https://doi.org/10.1016/j.epsl.2018.03.027

Arcay, D., Tric, E., & Doin, M.-P. (2007). Slab surface temperature in subduction zones: Influence of the interplate decoupling depth and upper plate thinning processes. *Earth and Planetary Science Letters*, *255*(3-4), 324–338. https://doi.org/10.1016/j.epsl.2006.12.027

Bachmann, F., Hielscher, R., & Schaeben, H. (2010). Texture analysis with mtex – free and open source software toolbox. *Solid State Phenomena*, *160*, 63–68. https://doi.org/10.4028/www.scientific.net/SSP.160.63

Bascou, J., Tommasi, A., & Mainprice, D. (2002). Plastic deformation and development of clinopyroxene lattice preferred orientations in eclogites. *Journal of Structural Geology*, *24*(8), 1357–1368. https://doi.org/10.1016/S0191-8141(01)00137-7

Bostock, M. G., Hyndman, R. D., Rondenay, S., & Peacock, S. M. (2002). An inverted continental Moho and serpentinization of the forearc mantle. *Nature*, *417*(6888), 536–538. https://doi.org/10.1038/417536a

Boudier, F., Ceuleneer, G., & Nicolas, A. (1988). Shear zones, thrusts and related magmatism in the Oman ophiolite: Initiation of thrusting on an oceanic ridge. *Tectonophysics*, *151*(1–4), 275–296. https://doi.org/10.1016/0040-1951(88)90249-1

Boudier, F., & Coleman, R. G. (1981). Cross section through the peridotite in the Samail ophiolite, southeastern Oman Mountains. *Journal of Geophysical Research*, *86*(B4), 2573–2592. https://doi.org/10.1029/JB086iB04p02573

Boullier, A. M., & Gueguen, Y. (1975). SP-mylonites: Origin of some mylonites by superplastic flow. *Contributions to Mineralogy and Petrology*, *50*(2), 93–104. https://doi.org/10.1007/BF00373329

Braun, J., Chéry, J., Poliakov, A., Mainprice, D., Vauchez, A., Tomassi, A., & Daignières, M. (1999). A simple parameterization of strain localization in the ductile regime due to grain size reduction: A case study for olivine. *Journal of Geophysical Research*, *104*(B11), 25,167–25,181. https://doi.org/10.1029/1999JB900214

Bucher, M. (1991). Mineral equilibria in metagabbros: Evidence for polymetamorphic evolution of the Asimah Window, northern Oman Mountains, United Arab Emirates. In *Ophiolite genesis and evolution of the oceanic lithosphere* (Vol. 5, pp. 543–571). Dordrecht, Netherlands: Springer. https://doi.org/10.1007/978-94-011-3358-6_27

Cao, Y., Jung, H., Song, S., Park, M., Jung, S., & Lee, J. (2015). Plastic deformation and seismic properties in fore-arc mantles: A petrofabric analysis of the Yushigou Harzburgites, North Qilian Suture Zone, NW China. *Journal of Petrology*, *56*(10), 1897–1944. https://doi.org/10.1093/petrology/egv053

Ceuleneer, G., Nicolas, A., & Boudier, F. (1988). Mantle flow patterns at an oceanic spreading centre: The Oman peridotites record. *Tectonophysics*, *151*(1–4), 1–26. https://doi.org/10.1016/0040-1951(88)90238-7

Chernak, L. J., & Hirth, G. (2010). Deformation of antigorite serpentinite at high temperature and pressure. *Earth and Planetary Science Letters*, *296*(1–2), 23–33. https://doi.org/10.1016/j.epsl.2010.04.035

Coleman, R. G. (1981). Tectonic setting for ophiolite obduction in Oman. *Journal of Geophysical Research*, *86*(B4), 2497–2508. https://doi.org/10.1029/JB086iB04p02497

Cowan, R. J., Searle, M. P., & Waters, D. J. (2014). Structure of the metamorphic sole to the Oman Ophiolite, Sumeini Window and Wadi Tayyin: Implications for ophiolite obduction processes. *Geological Society, London, Special Publications*, *392*(1), 155–175. https://doi.org/10.1144/SP392.8

De Ronde, A. A., & Stünitz, H. (2007). Deformation-enhanced reaction in experimentally deformed plagioclase-olivine aggregates. *Contributions to Mineralogy and Petrology*, *153*(6), 699–717. https://doi.org/10.1007/s00410-006-0171-7

De Ronde, A. A., Stünitz, H., Tullis, J., & Heilbronner, R. (2005). Reaction-induced weakening of plagioclase–olivine composites. *Tectonophysics*, *409*(1-4), 85–106. https://doi.org/10.1016/j.tecto.2005.08.008

Demouchy, S., Tommasi, A., Barou, F., Mainprice, D., & Cordier, P. (2012). Deformation of olivine in torsion under hydrous conditions. *Physics of the Earth and Planetary Interiors*, *202–203*, 56–70. https://doi.org/10.1016/j.pepi.2012.05.001

Dewey, J. F. (1976). Ophiolite obduction. *Tectonophysics*, *31*(1-2), 93–120. https://doi.org/10.1016/0040-1951(76)90169-4

Dewey, J. F., & Casey, J. F. (2013). The sole of an ophiolite: The Ordovician Bay of Islands Complex, Newfoundland. *Journal of the Geological Society*, *170*(5), 715–722. https://doi.org/10.1144/jgs2013-017

Dijkstra, A. H., Drury, M. R., Vissers, R. L., & Newman, J. (2002). On the role of melt-rock reaction in mantle shear zone formation in the Othris Peridotite Massif (Greece). *Journal of Structural Geology*, *24*(9), 1431–1450. https://doi.org/10.1016/S0191-8141(01)00142-0

Drury, M. R., Vissers, R. L., Van der Wal, D., & Strating, E. H. H. (1991). Shear localisation in upper mantle peridotites. *Pure and Applied Geophysics*, *137*(4), 439–460. https://doi.org/10.1007/BF00879044

Evans, B., Renner, J., & Hirth, G. (2001). A few remarks on the kinetics of static grain growth in rocks. *International Journal of Earth Sciences*, *90*(1), 88–103. https://doi.org/10.1007/s005310000150

Fryer, P., Wheat, C. G., & Mottl, M. J. (1999). Mariana blueschist mud volcanism: Implications for conditions within the subduction zone. *Geology*, *27*(2), 103–106. https://doi.org/10.1130/0091-7613(1999)027<0103:MBMVIF>2.3.CO;2

Furukawa, Y. (1993). Depth of the decoupling plate interface and thermal structure under arcs. *Journal of Geophysical Research*, *98*(B11), 20,005–20,013. https://doi.org/10.1029/93JB02020

Fusseis, F., Regenauer-Lieb, K., Liu, J., Hough, R. M., & De Carlo, F. (2009). Creep cavitation can establish a dynamic granular fluid pump in ductile shear zones. *Nature*, *459*(7249), 974–977. https://doi.org/10.1038/nature08051

Ghent, E. D., & Stout, M. Z. (1981). Metamorphism at the base of the Samail Ophiolite, southeastern Oman Mountains. *Journal of Geophysical Research*, *86*(B4), 2557–2571. https://doi.org/10.1029/JB086iB04p02557

Gnos, E. (1998). Peak metamorphic conditions of garnet amphibolites beneath the Semail Ophiolite: Implications for an inverted pressure gradient. *International Geology Review*, *40*(4), 281–304. https://doi.org/10.1080/00206819809465210

Gnos, E., & Kurz, D. (1994). Sapphirine-quartz and sapphirine-corundum assemblages in metamorphic rocks associated with the Semail Ophiolite (United Arab Emirates). *Contributions to Mineralogy and Petrology*, *116*(4), 398–410. https://doi.org/10.1007/BF00310907

Goodenough, K. M., Styles, M. T., Schofield, D., Thomas, R. J., Crowley, Q. C., Lilly, R. M., et al. (2010). Architecture of the Oman–UAE ophiolite: Evidence for a multi-phase magmatic history. *Arabian Journal of Geosciences*, *3*(4), 439–458. https://doi.org/10.1007/s12517-010-0177-3

Hacker, B. R., & Mosenfelder, J. L. (1996). Metamorphism and deformation along the emplacement thrust of the Samail ophiolite, Oman. *Earth and Planetary Science Letters*, *144*(3-4), 435–451. https://doi.org/10.1016/S0012-821X(96)00186-0

Hacker, B. R., Mosenfelder, J. L., & Gnos, E. (1996). Rapid emplacement of the Oman ophiolite: Thermal and geochronologic constraints. *Tectonics*, *15*(6), 1230–1247. https://doi.org/10.1029/96TC01973

Hansen, L. N., & Warren, J. M. (2015). Quantifying the effect of pyroxene on deformation of peridotite in a natural shear zone. *Journal of Geophysical Research: Solid Earth*, *120*, 2717–2738. https://doi.org/10.1002/2014JB011584

Harigane, Y., Michibayashi, K., Morishita, T., Tani, K., Dick, H. J. B., & Ishizuka, O. (2013). The earliest mantle fabrics formed during subduction zone infancy. *Earth and Planetary Science Letters*, *377–378*, 106–113. https://doi.org/10.1016/j.epsl.2013.06.031

Herwegh, M., Linckens, J., Ebert, A., Berger, A., & Brodhag, S. H. (2011). The role of second phases for controlling microstructural evolution in polymineralic rocks: A review. *Journal of Structural Geology*, *33*(12), 1728–1750. https://doi.org/10.1016/j.jsg.2011.08.011

Hidas, K., Tommasi, A., Garrido, C. J., Padrón-Navarta, J. A., Mainprice, D., Vauchez, A., et al. (2016). Fluid-assisted strain localization in the shallow subcontinental lithospheric mantle. *Lithos*, *262*, 636–650. https://doi.org/10.1016/j.lithos.2016.07.038

Hilairet, N., Reynard, B., Wang, Y., Daniel, I., Merkel, S., Nishiyama, N., & Petitgirard, S. (2007). High-pressure creep of serpentine, interseismic deformation, and initiation of subduction. *Science*, *318*(5858), 1910–1913. https://doi.org/10.1126/science.1148494

Hirth, G., & Guillot, S. (2013). Rheology and tectonic significance of serpentinite. *Elements*, *9*(2), 107–113. https://doi.org/10.2113/gselements.9.2.107

Hirth, G., & Kohlstedt, D. (2003). Rheology of the upper mantle and the mantle wedge: A view from the experimentalists. In J. Eiler (Ed.), *Inside the Subduction Factory*, *Geophysical Monograph Series*, (Vol. 138, pp. 83–105). Washington, DC: American Geophysical Union. https://doi.org/10.1029/138GM06

Holtzman, B. K., Kohlstedt, D. L., Zimmerman, M. E., Heidelbach, F., Hiraga, T., & Hustoft, J. (2003). Melt segregation and strain partitioning: Implications for seismic anisotropy and mantle flow. *Science*, *301*(5637), 1227–1230. https://doi.org/10.1126/science.1087132

Hyndman, R. D., & Peacock, S. M. (2003). Serpentinization of the forearc mantle. *Earth and Planetary Science Letters*, *212*(3–4), 417–432. https://doi.org/10.1016/S0012-821X(03)00263-2

Ishikawa, T., Fujisawa, S., Nagaishi, K., & Masuda, T. (2005). Trace element characteristics of the fluid liberated from amphibolite-facies slab: Inference from the metamorphic sole beneath the Oman ophiolite and implication for boninite genesis. *Earth and Planetary Science Letters*, *240*(2), 355–377. https://doi.org/10.1016/j.epsl.2005.09.049

Ismail, W. B., & Mainprice, D. (1998). An olivine fabric database: An overview of upper mantle fabrics and seismic anisotropy. *Tectonophysics*, *296*(1-2), 145–157. https://doi.org/10.1016/S0040-1951(98)00141-3

Jung, S., Jung, H., & Austrheim, H. (2014). Characterization of olivine fabrics and mylonite in the presence of fluid and implications for seismic anisotropy and shear localization. *Earth, Planets and Space*, *66*(1), 1–21.

Kaczmarek, M.-A., & Tommasi, A. (2011). Anatomy of an extensional shear zone in the mantle, Lanzo massif, Italy. *Geochemistry, Geophysics, Geosystems*, *12*, Q0AG06. https://doi.org/10.1029/2011GC003627

Karato, S.-I., & Wu, P. (1993). Rheology of the upper mantle: A synthesis. *Science*, *260*(5109), 771–778. https://doi.org/10.1126/science.260.5109.771

Katayama, I., Jung, H., & Karato, S. (2004). New type of olivine fabric from deformation experiments at modest water content and low stress. *Geology*, *32*(12), 1045–1048. https://doi.org/10.1130/G20805.1

Kawakatsu, H., & Watada, S. (2007). Seismic evidence for deep-water transportation in the mantle. *Science*, *316*(5830), 1468–1471. https://doi.org/10.1126/science.1140855

Kelemen, P. B., & Dick, H. J. (1995). Focused melt flow and localized deformation in the upper mantle: juxtaposition of replacive dunite and ductile shear zones in the Josephine peridotite, SW Oregon. *Journal of Geophysical Research: Solid Earth*, *100*(B1), 423–438. https://doi.org/10.1029/94JB02063

Kelemen, P. B., Rilling, J. L., Parmentier, E. M., Mehl, L., & Hacker, B. R. (2003). Thermal structure due to solid-state flow in the mantle wedge beneath arcs. *Inside the Subduction Factory*, 293–311. https://doi.org/10.1029/138GM13

Khedr, M. Z., Arai, S., & Python, M. (2013). Petrology and chemistry of basal lherzolites above the metamorphic sole from Wadi Sarami central Oman ophiolite. *Journal of Mineralogical and Petrological Sciences*, *108*(1), 13–24. https://doi.org/10.2465/jmps.121026

Khedr, M. Z., Arai, S., Python, M., & Tamura, A. (2014). Chemical variations of abyssal peridotites in the central Oman ophiolite: Evidence of oceanic mantle heterogeneity. *Gondwana Research*, *25*(3), 1242–1262. https://doi.org/10.1016/j.gr.2013.05.010

Kilian, R., Heilbronner, R., & Stünitz, H. (2011). Quartz grain size reduction in a granitoid rock and the transition from dislocation to diffusion creep. *Journal of Structural Geology*, *33*(8), 1265–1284. https://doi.org/10.1016/j.jsg.2011.05.004

Le Mée, L., Girardeau, J., & Monnier, C. (2004). Mantle segmentation along the Oman ophiolite fossil mid-ocean ridge. *Nature*, *432*(7014), 167–172. https://doi.org/10.1038/nature03075

Lemarchand, D., Cividini, D., Turpault, M.-P., & Chabaux, F. (2012). Boron isotopes in different grain size fractions: Exploring past and present water–rock interactions from two soil profiles (Strengbach, Vosges Mountains). *Geochimica et Cosmochimica Acta*, *98*, 78–93. https://doi.org/10.1016/j.gca.2012.09.009

Linckens, J., Bruijn, R. H., & Skemer, P. (2014). Dynamic recrystallization and phase mixing in experimentally deformed peridotite. *Earth and Planetary Science Letters*, *388*, 134–142. https://doi.org/10.1016/j.epsl.2013.11.037

Linckens, J., Herwegh, M., & Müntener, O. (2011). Linking temperature estimates and microstructures in deformed polymineralic mantle rocks. *Geochemistry, Geophysics, Geosystems*, *12*, Q08004. https://doi.org/10.1029/2011GC003536

Linckens, J., Herwegh, M., Müntener, O., & Mercolli, I. (2011). Evolution of a polymineralic mantle shear zone and the role of second phases in the localization of deformation. *Journal of Geophysical Research*, *116*, B06210. https://doi.org/10.1029/2010JB008119

Linckens, J., Herwegh, M., & Müntener, O. (2015). Small quantity but large effect—How minor phases control strain localization in upper mantle shear zones. *Tectonophysics*, *643*, 26–43. https://doi.org/10.1016/j.tecto.2014.12.008

Lippard, S. J., Shelton, A. W., & Gass, I. G. (1986). *The ophiolite of northern Oman*, *Memoir* (Vol. 11). London: Geological Society.

Mainprice, D., Bachmann, F., Hielscher, R., & Schaeben, H. (2014). Descriptive tools for the analysis of texture projects with large datasets using MTEX: Strength, symmetry and components. *Geological Society, London, Special Publications*, *409*(1), 251–271. https://doi.org/10.1144/SP409.8

Mainprice, D., & Silver, P. G. (1993). Interpretation of SKS-waves using samples from the subcontinental lithosphere. *Physics of the Earth and Planetary Interiors*, *78*(3–4), 257–280. https://doi.org/10.1016/0031-9201(93)90160-B

Mancktelow, N. S., Grujic, D., & Johnson, E. L. (1998). An SEM study of porosity and grain boundary microstructure in quartz mylonites, Simplon Fault Zone, Central Alps. *Contributions to Mineralogy and Petrology*, *131*(1), 71–85. https://doi.org/10.1007/s004100050379

Marschall, H. R., Wanless, V. D., Shimizu, N., Pogge von Strandmann, P. A. E., Elliott, T., & Monteleone, B. D. (2017). The boron and lithium isotopic composition of mid-ocean ridge basalts and the mantle. *Geochimica et Cosmochimica Acta*, *207*, 102–138. https://doi.org/10.1016/j.gca.2017.03.028

Mehl, L., Hacker, B. R., Hirth, G., & Kelemen, P. B. (2003). Arc-parallel flow within the mantle wedge: Evidence from the accreted Talkeetna arc, south central Alaska. *Journal of Geophysical Research*, *108*(B8), 2375. https://doi.org/10.1029/2002JB002233

Menegon, L., Fusseis, F., Stünitz, H., & Xiao, X. (2015). Creep cavitation bands control porosity and fluid flow in lower crustal shear zones. *Geology*, *43*(3), 227–230. https://doi.org/10.1130/G36307.1

Michibayashi, K., Gerbert-Gaillard, L., & Nicolas, A. (2000). Shear sense inversion in the Hilti mantle section (Oman ophiolite) and active mantle uprise. *Marine Geophysical Researches*, *21*(3/4), 259–268. https://doi.org/10.1023/A:1026713909204

Michibayashi, K., Ina, T., & Kanagawa, K. (2006). The effect of dynamic recrystallization on olivine fabric and seismic anisotropy: Insight from a ductile shear zone, Oman ophiolite. *Earth and Planetary Science Letters*, *244*(3–4), 695–708. https://doi.org/10.1016/j.epsl.2006.02.019

Michibayashi, K., & Mainprice, D. (2004). The role of pre-existing mechanical anisotropy on shear zone development within oceanic mantle lithosphere: An example from the Oman Ophiolite. *Journal of Petrology*, *45*(2), 405–414. https://doi.org/10.1093/petrology/egg099

Michibayashi, K., Mainprice, D., Fujii, A., Uehara, S., Shinkai, Y., Kondo, Y., et al. (2016). Natural olivine crystal-fabrics in the western Pacific convergence region: A new method to identify fabric type. *Earth and Planetary Science Letters*, *443*, 70–80. https://doi.org/10.1016/j.epsl.2016.03.019

Michibayashi, K., Ohara, Y., Stern, R. J., Fryer, P., Kimura, J.-I., Tasaka, M., et al. (2009). Peridotites from a ductile shear zone within back-arc lithospheric mantle, southern Mariana Trench: Results of a Shinkai 6500 dive. *Geochemistry, Geophysics, Geosystems*, *10*, Q05X06. https://doi.org/10.1029/2008GC002197

Michibayashi, K., & Oohara, T. (2013). Olivine fabric evolution in a hydrated ductile shear zone at the Moho transition zone, Oman Ophiolite. *Earth and Planetary Science Letters*, *377–378*, 299–310. https://doi.org/10.1016/j.epsl.2013.07.009

Morris, A., Meyer, M., Anderson, M. W., & MacLeod, C. J. (2016). Clockwise rotation of the entire Oman ophiolite occurred in a suprasubduction zone setting. *Geology*, *44*(12), 1055–1058. https://doi.org/10.1130/G38380.1

Naze, L., Doukhan, N., Doukhan, J.-C., & Latrous, K. (1987). A TEM study of lattice defects in naturally and experimentally deformed orthopyroxenes. *Bulletin de Mineralogie*, *110*(5), 497–512.

Newman, J., Lamb, W. M., Drury, M. R., & Vissers, R. L. (1999). Deformation processes in a peridotite shear zone: Reaction-softening by an H_2O-deficient, continuous net transfer reaction. *Tectonophysics*, *303*(1-4), 193–222. https://doi.org/10.1016/S0040-1951(98)00259-5

Nicolas, A., Boudier, F., Ildefonse, B., & Ball, E. (2000). Accretion of Oman and United Arab Emirates ophiolite—Discussion of a new structural map. *Marine Geophysical Researches*, *21*(3/4), 147–180. https://doi.org/10.1023/A:1026769727917

Obara, K. (2002). Nonvolcanic deep tremor associated with subduction in southwest Japan. *Science*, *296*(5573), 1679–1681. https://doi.org/10.1126/science.1070378

Peacock, S. M. (1996). Thermal and petrologic structure of subduction zones. In *Subduction: Top to bottom*, *Geophysical Monograph Series* (Vol. 96, pp. 119–133). Washington, DC: American Geophysical Union.

Peacock, S. M., & Hyndman, R. D. (1999). Hydrous minerals in the mantle wedge and the maximum depth of subduction thrust earthquakes. *Geophysical Research Letters*, *26*(16), 2517–2520. https://doi.org/10.1029/1999GL900558

Précigout, J., & Gueydan, F. (2009). Mantle weakening and strain localization: Implications for the long-term strength of the continental lithosphere. *Geology*, *37*(2), 147–150. https://doi.org/10.1130/G25239A.1

Précigout, J., Prigent, C., Palasse, L., & Pochon, A. (2017). Water pumping in mantle shear zones. *Nature Communications*, *8*(15736). https://doi.org/10.1038/ncomms15736

Précigout, J., & Stünitz, H. (2016). Evidence of phase nucleation during olivine diffusion creep: A new perspective for mantle strain localisation. *Earth and Planetary Science Letters*, *455*, 94–105. https://doi.org/10.1016/j.epsl.2016.09.029

Prigent, C., Guillot, S., Agard, P., Lemarchand, D., Soret, M., & Ulrich, M. (2018). Transfer of subduction fluids into the deforming mantle wedge during nascent subduction: Evidence from trace elements and boron isotopes (Semail ophiolite, Oman). *Earth and Planetary Science Letters*, *484*, 213–228. https://doi.org/10.1016/j.epsl.2017.12.008

Raleigh, C. B., & Paterson, M. S. (1965). Experimental deformation of serpentinite and its tectonic implications. *Journal of Geophysical Research*, *70*(16), 3965–3985. https://doi.org/10.1029/JZ070i016p03965

Regenauer-Lieb, K., Yuen, D. A., & Branlund, J. (2001). The initiation of subduction: Criticality by addition of water? *Science*, *294*(5542), 578–580. https://doi.org/10.1126/science.1063891

Reynard, B. (2013). Serpentine in active subduction zones. *Lithos*, *178*, 171–185. https://doi.org/10.1016/j.lithos.2012.10.012

Rioux, M., Bowring, S., Kelemen, P., Gordon, S., Miller, R., & Dudás, F. (2013). Tectonic development of the Samail ophiolite: High-precision U-Pb zircon geochronology and Sm-Nd isotopic constraints on crustal growth and emplacement. *Journal of Geophysical Research: Solid Earth*, *118*, 2085–2101. https://doi.org/10.1002/jgrb.50139

Rioux, M., Garber, J., Bauer, A., Bowring, S., Searle, M., Kelemen, P., & Hacker, B. (2016). Synchronous formation of the metamorphic sole and igneous crust of the Semail ophiolite: New constraints on the tectonic evolution during ophiolite formation from high-precision U–Pb zircon geochronology. *Earth and Planetary Science Letters*, *451*, 185–195. https://doi.org/10.1016/j.epsl.2016.06.051

Rybacki, E., Wirth, R., & Dresen, G. (2008). High-strain creep of feldspar rocks: Implications for cavitation and ductile failure in the lower crust. *Geophysical Research Letters*, *35*, L04304. https://doi.org/10.1029/2007GL032478

Searle, M. P. (1980). The metamorphic sheet and underlying volcanic rocks beneath the Semail ophiolite in the northern Oman Mountains of Arabia. Open University.

Searle, M. P., & Cox, J. (1999). Tectonic setting, origin, and obduction of the Oman ophiolite. *Geological Society of America Bulletin*, *111*(1), 0104–0122. https://doi.org/10.1130/0016-7606(1999)111<0104:TSOAOO>2.3.CO;2

Searle, M. P., & Cox, J. (2002). Subduction zone metamorphism during formation and emplacement of the Semail ophiolite in the Oman Mountains. *Geological Magazine*, *139*(03), 241–255.

Searle, M. P., & Malpas, J. (1980). Structure and metamorphism of rocks beneath the Semail ophiolite of Oman and their significance in ophiolite obduction. *Earth and Environmental Science Transactions of the Royal Society of Edinburgh*, *71*(04), 247–262. https://doi.org/10.1017/S0263593300013614

Searle, M. P., & Malpas, J. (1982). Petrochemistry and origin of sub-ophiolitic metamorphic and related rocks in the Oman Mountains. *Journal of the Geological Society*, *139*(3), 235–248. https://doi.org/10.1144/gsjgs.139.3.0235

Skemer, P., Katayama, I., Jiang, Z., & Karato, S. (2005). The misorientation index: Development of a new method for calculating the strength of lattice-preferred orientation. *Tectonophysics*, *411*(1-4), 157–167. https://doi.org/10.1016/j.tecto.2005.08.023

Soret, M., Agard, P., Dubacq, B., Plunder, A., & Yamato, P. (2017). Petrological evidence for stepwise accretion of metamorphic soles during subduction infancy (Semail ophiolite, Oman and UAE). *Journal of Metamorphic Geology*, *35*(9), 1051–1080. https://doi.org/10.1111/jmg.12267

Soustelle, V., Tommasi, A., Demouchy, S., & Ionov, D. A. (2010). Deformation and fluid–rock interaction in the supra-subduction mantle: Microstructures and water contents in peridotite xenoliths from the Avacha Volcano, Kamchatka. *Journal of Petrology*, *51*(1–2), 363–394. https://doi.org/10.1093/petrology/egp085

Spray, J. G. (1984). Possible causes and consequences of upper mantle decoupling and ophiolite displacement. *Geological Society, London, Special Publications*, *13*(1), 255–268. https://doi.org/10.1144/GSL.SP.1984.013.01.21

Steuten, J. M., & Van Roermund, H. L. M. (1989). An optical and electron microscopy study of defect structures in naturally deformed orthopyroxene. *Tectonophysics*, *157*(4), 331–338. https://doi.org/10.1016/0040-1951(89)90148-0

Stevenson, D. J. (1989). Spontaneous small-scale melt segregation in partial melts undergoing deformation. *Geophysical Research Letters*, *16*(9), 1067–1070. https://doi.org/10.1029/GL016i009p01067

Suhr, G. (1993). Evaluation of upper mantle microstructures in the Table Mountain massif (Bay of Islands ophiolite). *Journal of Structural Geology*, *15*(11), 1273–1292. https://doi.org/10.1016/0191-8141(93)90102-G

Syracuse, E. M., van Keken, P. E., & Abers, G. A. (2010). The global range of subduction zone thermal models. *Physics of the Earth and Planetary Interiors*, *183*(1–2), 73–90. https://doi.org/10.1016/j.pepi.2010.02.004

Takazawa, E., Okayasu, T., & Satoh, K. (2003). Geochemistry and origin of the basal lherzolites from the northern Oman ophiolite (northern Fizh block). *Geochemistry, Geophysics, Geosystems*, *4*(2), 1021. https://doi.org/10.1029/2001GC000232

Tasaka, M., & Hiraga, T. (2013). Influence of mineral fraction on the rheological properties of forsterite + enstatite during grain-size-sensitive creep: 1. Grain size and grain growth laws. *Journal of Geophysical Research: Solid Earth*, *118*, 3970–3990. https://doi.org/10.1002/jgrb.50285

Tasaka, M., Hiraga, T., & Michibayashi, K. (2014). Influence of mineral fraction on the rheological properties of forsterite + enstatite during grain size sensitive creep: 3. Application of grain growth and flow laws on peridotite ultramylonite. *Journal of Geophysical Research: Solid Earth*, *119*, 840–857. https://doi.org/10.1002/2013JB010619

Tasaka, M., Zimmerman, M. E., Kohlstedt, D. L., Stünitz, H., & Heilbronner, R. (2017). Rheological weakening of olivine+ orthopyroxene aggregates due to phase mixing: Part 2. Microstructural development. *Journal of Geophysical Research: Solid Earth*, *122*, 7597–7612. https://doi.org/10.1002/2017JB014311

Tommasi, A., & Vauchez, A. (2015). Heterogeneity and anisotropy in the lithospheric mantle. *Tectonophysics*, *661*, 11–37. https://doi.org/10.1016/j.tecto.2015.07.026

Tommasi, A., Vauchez, A., Fernandes, L. A., & Porcher, C. C. (1994). Magma-assisted strain localization in an orogen-parallel. *Tectonics*, *13*(2), 421–437. https://doi.org/10.1029/93TC03319

Tommasi, A., Vauchez, A., Godard, M., & Belley, F. (2006). Deformation and melt transport in a highly depleted peridotite massif from the Canadian Cordillera: Implications to seismic anisotropy above subduction zones. *Earth and Planetary Science Letters*, *252*(3–4), 245–259. https://doi.org/10.1016/j.epsl.2006.09.042

Toy, V. G., Newman, J., Lamb, W., & Tikoff, B. (2010). The role of pyroxenites in formation of shear instabilities in the mantle: Evidence from an ultramafic ultramylonite, Twin Sisters Massif, Washington. *Journal of Petrology*, *51*(1–2), 55–80. https://doi.org/10.1093/petrology/egp059

van Keken, P. E., Kiefer, B., & Peacock, S. M. (2002). High-resolution models of subduction zones: Implications for mineral dehydration reactions and the transport of water into the deep mantle. *Geochemistry, Geophysics, Geosystems*, *3*(10), 1056. https://doi.org/10.1029/2001GC000256

Van Roermund, H. L. M., & Boland, J. N. (1981). The dislocation substructures of naturally deformed omphacites. *Tectonophysics*, *78*(1–4), 403–418. https://doi.org/10.1016/0040-1951(81)90022-6

Vissers, R. L. M., Drury, M. R., Hoogerduijn, E. H., Spiers, C. J., & Van der Wal, D. (1995). Mantle shear zones and their effect on lithosphere strength during continental breakup. *Tectonophysics*, *249*(3-4), 155–171. https://doi.org/10.1016/0040-1951(95)00033-J

Wada, I., & Wang, K. (2009). Common depth of slab-mantle decoupling: Reconciling diversity and uniformity of subduction zones. *Geochemistry, Geophysics, Geosystems*, *10*, Q10009. https://doi.org/10.1029/2009GC002570

Wada, I., Wang, K., He, J., & Hyndman, R. D. (2008). Weakening of the subduction interface and its effects on surface heat flow, slab dehydration, and mantle wedge serpentinization. *Journal of Geophysical Research*, *113*, B04402. https://doi.org/10.1029/2007JB005190

Wakabayashi, J., & Dilek, Y. (2003). What constitutes "emplacement" of an ophiolite?: Mechanisms and relationship to subduction initiation and formation of metamorphic soles. *Geological Society, London, Special Publications*, *218*(1), 427–447. https://doi.org/10.1144/GSL.SP.2003.218.01.22

Wark, D. A., & Watson, E. B. (2000). Effect of grain size on the distribution and transport of deep-seated fluids and melts. *Geophysical Research Letters*, *27*(14), 2029–2032. https://doi.org/10.1029/2000GL011503

Warren, C. J., Parrish, R. R., Waters, D. J., & Searle, M. P. (2005). Dating the geologic history of Oman's Semail ophiolite: Insights from U-Pb geochronology. *Contributions to Mineralogy and Petrology*, *150*(4), 403–422. https://doi.org/10.1007/s00410-005-0028-5

Warren, J. M., & Hirth, G. (2006). Grain size sensitive deformation mechanisms in naturally deformed peridotites. *Earth and Planetary Science Letters*, *248*(1-2), 438–450. https://doi.org/10.1016/j.epsl.2006.06.006

Yoshikawa, M., Python, M., Tamura, A., Arai, S., Takazawa, E., Shibata, T., et al. (2015). Melt extraction and metasomatism recorded in basal peridotites above the metamorphic sole of the northern Fizh massif, Oman ophiolite. *Tectonophysics*, *650*, 53–64. https://doi.org/10.1016/j.tecto.2014.12.004

Zhang, J., Green, H. W. II, & Bozhilov, K. N. (2006). Rheology of omphacite at high temperature and pressure and significance of its lattice preferred orientations. *Earth and Planetary Science Letters*, *246*(3–4), 432–443. https://doi.org/10.1016/j.epsl.2006.04.006